nature electronics

ARTICLES

https://doi.org/10.1038/s41928-021-00685-8

Healing of donor defect states in monolayer molybdenum disulfide using oxygen-incorporated chemical vapour deposition

Pin-Chun Shen[1,8], Yuxuan Lin[1,8], Cong Su[2], Christina McGahan[3], Ang-Yu Lu[1], Xiang Ji[1], Xingzhi Wang[4], Haozhe Wang[1], Nannan Mao[1,5], Yunfan Guo[1], Ji-Hoon Park[1], Yan Wang[6], William Tisdale[5], Ju Li[2], Xi Ling[4,7], Katherine E. Aidala[3], Tomás Palacios[1] and Jing Kong[1] ✉

Two-dimensional molybdenum disulfide (MoS_2) is a semiconductor that could be used to build scaled transistors and other advanced electronic and optoelectronic devices. However, the material typically exhibits strong n-type doping, low photoluminescence quantum yields and high contact resistance with metals, behaviour that is often attributed to the presence of donor states induced by sulfur vacancies. Here we show that oxygen-incorporated chemical vapour deposition can be used to passivate sulfur vacancies and suppress the formation of donor states in monolayer MoS_2. First-principles calculations and spectroscopy measurements are used to reveal the formation of molybdenum–oxygen bonding at the sulfur vacancy sites and the absence of donor states in oxygen-incorporated MoS_2. Compared with MoS_2 fabricated via chemical vapour deposition without oxygen, oxygen-incorporated MoS_2 exhibits enhanced photoluminescence, higher work function and improved contact resistance with a lower Schottky barrier (less than 40 meV) at the metal/MoS_2 interface.

The semiconductor industry relies on engineering the electronic and optical properties of semiconductor crystals—without degrading performance—using techniques such as doping[1], stoichiometry[2], defect engineering[3] and interfacial effects[4]. Transition metal dichalcogenides (TMDs), such as monolayer molybdenum disulfide (MoS_2), has been proposed as an alternative semiconductor to silicon due to their bandgap (1.8−1.9 eV), moderate carrier mobility and atomically thin body (6.5 Å), which is ideal for gate electrostatic control and device downscaling[5]. However, the thinness of TMD monolayers also makes them highly susceptible to intrinsic and extrinsic defects and impurities[6,7]. It has, in particular, been theoretically predicted and experimentally observed that the electron transport and excitonic transitions of MoS_2 are strongly affected by defects[7,8], strain[9] and substrate effects[10].

Sulfur vacancies (V_S) are the most commonly observed natural structural defects in MoS_2 due to their lower formation energy compared with other structural defects[11,12], and typical densities of V_S in monolayer MoS_2 can be up to 10^{13} cm^{-2} (ref. [13]). These vacancies induce defect states localized below the conduction band minimum (CBM) of MoS_2 (refs. [14,15]) and can be detrimental to the performance of electronic and optoelectronic devices, acting as scattering centres that limit carrier mobility[7,8], and mediating non-radiative recombinations that reduce the photoluminescence (PL) efficiency[16,17]. In addition, V_S can function as electron donors due to unsaturated bonds, resulting in strong electron (n-type) doping in monolayer MoS_2 (ref. [18]). As a result, PL intensity is decreased due to quenching of the optical transitions of neutral excitons and formation of charged excitions (trions) in electron-rich environments[17,19]. When in contact with metals, V_S-induced defect states in the bandgap cause Fermi-level pinning, resulting in high Schottky barriers[14,20–22]. The Schottky barrier height (SBH) at metal/MoS_2 interfaces is typically in the range of 100−400 meV (refs. [22–27]), which impedes electronic transport and results in poor electrical contact resistance (R_C). Thus, to improve the performance of MoS_2-based electronic and optoelectronic devices, approaches to passivate the V_S in the material are required.

Doping and defect engineering in MoS_2 are, however, challenging due to its low dimensionality. The V_S can be physically passivated through surface modification, such as superacid treatment[16], thiol chemistry modification[28] and oxygen physio-adsorption[29,30]. These physical treatment methods can repair the V_S and reduce the density of trap states, thus enhancing the exciton emission efficiency and electron mobility in MoS_2. Though surface modifications by molecules and ions can locally alter the electronic and optoelectronic properties, these treatments suffer from chemical instability and incompatibility with device fabrication processes. Several chemical treatment approaches have also been developed, such as high-temperature annealing in a sulfur-rich or oxygen-rich environment[30,31], laser-irradiation-assisted oxygen adsorption[32], and ion radiation and plasma treatment[33–35]. These methods are more stable than surface modification, but crystallinity and uniformity are inevitably compromised.

In this Article, we report a scalable oxygen-incorporated chemical vapour deposition (O_2-CVD) technique that can suppress the formation of donor defect states in monolayer MoS_2. Using density functional theory (DFT) calculations, the presence of oxygen at the V_S sites is shown to passivate the V_S-induced donor energy levels and reduce undesired n-type doping, as well as preserving

[1]Department of Electrical Engineering and Computer Science, Massachusetts Institute of Technology, Cambridge, MA, USA. [2]Department of Nuclear Science and Engineering, Massachusetts Institute of Technology, Cambridge, MA, USA. [3]Department of Physics, Mount Holyoke College, South Hadley, MA, USA. [4]Department of Chemistry, Boston University, Boston, MA, USA. [5]Department of Chemical Engineering, Massachusetts Institute of Technology, Cambridge, MA, USA. [6]Institute of Microelectronics, Tsinghua University, Beijing, China. [7]Division of Materials Science and Engineering, Boston University, Boston, MA, USA. [8]These authors contributed equally: Pin-Chun Shen, Yuxuan Lin. ✉e-mail: jingkong@mit.edu

the electronic band structure and carrier mobility. Electron depletion of the passivated MoS_2 is confirmed by Raman, PL, X-ray photoelectron spectroscopy (XPS) and electrostatic force microscopy (EFM), as well as by the shift in the threshold voltage of MoS_2 transistors. We also show enhanced PL emissions due to reduced non-radiative recombinations and electron depletion, reduction in Schottky barrier (<40 meV) and improvement in contact resistance at the metal/MoS_2 interface (1 kΩ µm), which is due to suppression of the defect-induced Fermi-level pinning effect. Gate-dependent PL measurements at low temperature show an absence of donor-defect-bound excitons in the oxygen-incorporated MoS_2, compared with CVD-grown MoS_2 without oxygen incorporation.

Deposition of monolayer MoS_2 with oxygen

To study the effects of oxygen in the growth environment on the performance of MoS_2, three conditions are designed and used to obtain three distinct types of monolayer MoS_2 crystal, namely, oxygen-incorporated MoS_2 (O-MoS_2), MoS_2 grown under the sulfur-mild condition (SM-MoS_2) and MoS_2 grown under the sulfur-excess condition (SE-MoS_2). Typical optical microscopy images are shown in Fig. 1a–c. These three types of MoS_2 crystal are deposited on 300 nm SiO_2/Si substrates at 625 °C for 3 min through the sulfurization of molybdenum trioxide (MoO_3) powder using our previously reported perylene-3,4,9,10-tetracarboxylic acid tetrapotassium (PTAS)-molecules-assisted CVD method[36]. Besides the carrier gas of Ar, an additional flow of oxygen gas is introduced during deposition to provide the oxygen source. The experimental CVD setup and detailed growth conditions are provided in Supplementary Section 1. For typical CVD of MoS_2 grown without oxygen, triangular shapes are dominantly present at the optimized sulfur-mild condition (SM-MoS_2; Fig. 1a) (O_2, 0 s.c.c.m.; S, 20 mg; MoO_3, 20 mg), whereas a sulfur-rich condition (O_2, 0 s.c.c.m.; S, 40 mg; MoO_3, 20 mg) yields concave MoS_2 crystals whose edges are inwardly curved (SE-MoS_2; Fig. 1b), reflecting the mismatch of the growth rate at the crystal edges owing to the highly unbalanced precursor ratio during the growth[37]. These two flake types represent the most common MoS_2 crystals obtained through CVD methods[7,36,38–41].

According to the Mo–O–S ternary phase diagram (Fig. 1e), the presence of moderate amounts of oxygen in the O_2-CVD system could offer a chemical path to obtain partially oxidized MoS_2 (referred to as O-MoS_2 in this work). Additionally, PTAS-assisted CVD allows the growth of O-MoS_2 crystals at a lower temperature with a shorter deposition time[36], which avoids the anisotropic oxidative etching of MoS_2 previously reported (850 °C, >30 min)[42]. We note that the presence of oxygen tends to shape the crystals into a convex geometry (Fig. 1c; O_2, 0.2 s.c.c.m.; S, 20 mg; MoO_3, 20 mg), which has not been revealed in a previous study[42], indicating a different growth regime in our study. Supplementary Fig. 2 shows that the crystal geometries undergo a clear evolution from triangular to hexagonal and then to circular as the flow rate of oxygen increases. Within our proposed process windows, no etching effects on the as-grown crystals are observed. Previous theoretical work has shown that these convex crystal geometries are more energetically favourable in a sulfur-deficient growth condition because the formation energies of various edge configurations such as Mo zigzag edge, S zigzag edge and armchair can be nearly equivalent in such a growth environment, whereas S zigzag edges have less formation energies in a sulfur-rich environment, resulting in a triangular shape[43]. A thickness below 1 nm characterized by atomic force microscopy confirms that the as-grown O-MoS_2 crystals are monolayer (Supplementary Fig. 3d). Second-harmonic generation measurements reveal that the individual O-MoS_2 domain is single crystalline without grain boundaries (Supplementary Section 2 provides further details)[44]. To clarify the structure of monolayer O-MoS_2, transmission electron microscopy (TEM) characterization is carried out (Fig. 1f,g). The selected-area electron diffraction pattern for the as-grown monolayer O-MoS_2 (Fig. 1g) shows a set of sixfold-symmetric diffraction points, corresponding to the monolayer hexagonal lattice structure of MoS_2 (ref. [39]). In addition to O-MoS_2, layered MoO_2 can also be formed when a high flow rate of oxygen (O_2, 2 s.c.c.m.; S, 20 mg; MoO_3, 20 mg) is introduced (Fig. 1d). The lack of gate dependence and high conductivity shown in Supplementary Fig. 4b,c reveal the metallic nature of these CVD-grown layered MoO_2 crystals.

XPS measurements confirm the presence of Mo–O bonds and less n-type doping in the as-grown O-MoS_2. The peak located at 530.3 eV in the O 1*s* spectra as well as the two well-pronounced MoO_x-related peaks at 232.3 and 235.4 eV for Mo(VI) $3d_{5/2}$ and Mo(VI) $3d_{3/2}$ in the Mo 3*d* spectra[30,45,46] (Fig. 1h,i), respectively, signify the existence of covalent Mo–O bonds in the O-MoS_2 sample. These Mo–O bonds may originate from either oxygen-passivated sulfur vacancies in MoS_2 or residual clusters of MoO_x during growth; therefore, before XPS characterization, the O-MoS_2 sample is carefully rinsed by deionized water and isopropyl alcohol to remove MoO_x on the surface. Importantly, the XPS data of O-MoS_2 exhibit a redshift in binding energies for both Mo(IV) $3d_{5/2}$ from 229.7 to 229.4 eV and S 2*s* from 226.7 to 226.4 eV (Fig. 1h). Similar shifts are also observed for the S2*p* peaks (Supplementary Fig. 8). The binding-energy redshifts can be translated to a downward shift of 0.3 eV of the Fermi level in O-MoS_2, that is, the Fermi level moves towards the valence band maximum, indicating less n-type doping[47]. These observations suggest the electron depletion of the as-grown monolayer O-MoS_2 crystals as compared with regular CVD MoS_2 crystals.

Reduction in n-type doping of O-MoS_2

The first effect of oxygen on the as-grown O-MoS_2 crystals is PL enhancement. Figure 2a compares the room-temperature PL spectra of three types of monolayer MoS_2. The distinct PL peaks at 1.8–1.9 eV and the absence of indirect emission peaks at lower energies confirm that the as-grown MoS_2 crystals are monolayer[48]. Similar to previous studies on surface-defect-passivation treatment[16], p-type chemical doping[19] or electrostatic hole doping[17] of MoS_2, the O-MoS_2 crystals also exhibit an enhanced PL with a higher peak energy of 1.87 eV. In contrast, the PL intensity decreases and PL peak shifts towards a lower energy with an increased amount of sulfur involved during the growth (1.85 and 1.83 eV for SM-MoS_2 and SE-MoS_2, respectively). The PL of MoS_2 at room temperature is mainly attributed to the radiative optical transitions of neutral excitons and trions and is highly sensitive to doping and impurities[17,19,48]. The blueshift in the PL peak in O-MoS_2 suggests that the neutral excitons are much more populated than trions in the crystals[17,19], a common sign of less n-type doping and fewer defect states. This also results in the suppression of non-radiative recombination and enhanced PL intensity. The emission energy difference between O-MoS_2 and SM- or SE-MoS_2 samples can be observed more clearly on the PL mapping results, where the O-MoS_2 flake (Fig. 2a,c) has a PL emission energy of 1.87 eV, corresponding to neutral A-exciton emission[48], whereas both SM-MoS_2 and SE-MoS_2 crystals exhibit lower PL emission energies at around 1.84 and 1.82 eV, respectively (Fig. 2a,d,e), indicating their trion-dominated characteristics.

Raman spectroscopy is carried out to quantitatively characterize the doping concentration. The distributions of doping concentration and strain can be simultaneously extracted from the Raman shifts of the two vibrational modes (Supplementary Section 4)[10,49,50]. As shown in Fig. 2b, the as-grown O-MoS_2 exhibits a blueshift in the A_{1g} vibrational mode as opposed to those in both SM-MoS_2 and SE-MoS_2, which can be translated into a lower electron concentration[10,51]. The spatial distributions of change in electron concentrations extracted from the Raman shifts are shown in Fig. 2f–h. For the MoS_2 crystals grown in typical CVD environments without oxygen (namely, SM-MoS_2 and SE-MoS_2), high levels of n-type doping

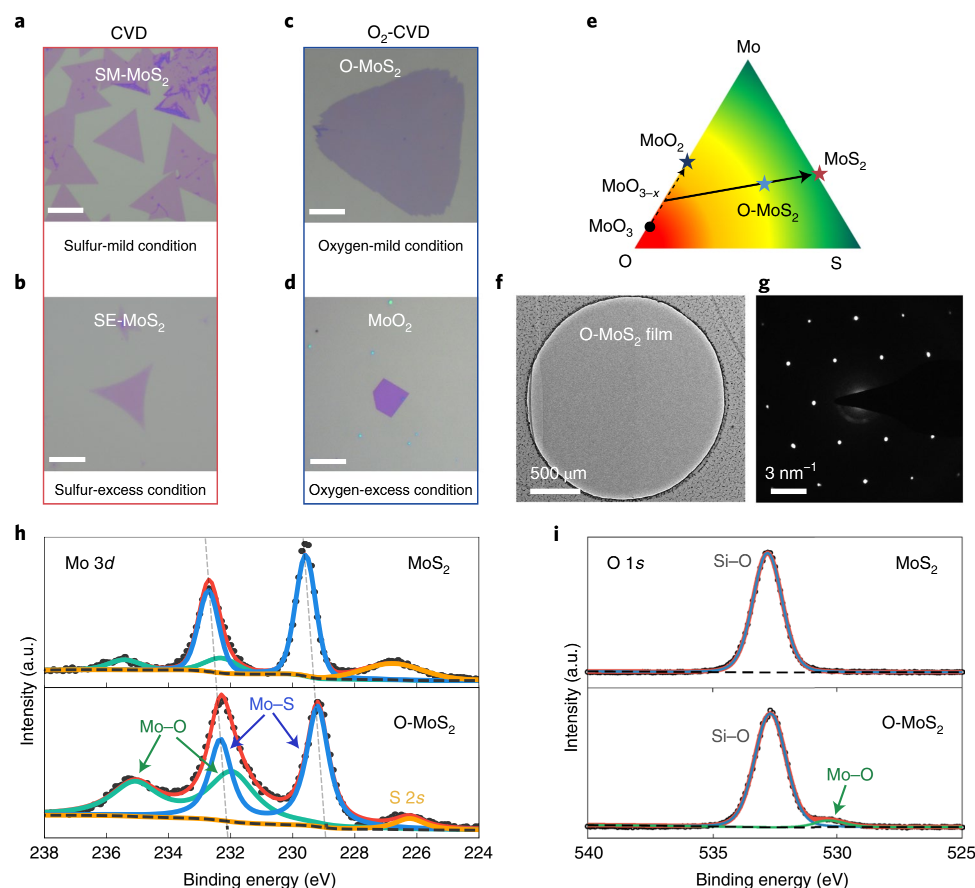

Fig. 1 | Deposition of monolayer MoS_2 with and without oxygen incorporation. a, Optical image of a typical monolayer MoS_2 crystal grown without oxygen under the sulfur-mild condition, showing a triangular shape. **b**, Optical image of a monolayer MoS_2 crystal grown without oxygen under a sulfur-excess condition. The crystal shows inward curved edges (concave shape). **c**, Optical image of a monolayer MoS_2 grown in an oxygen-mild environment. The crystal shows outward curved edges (convex shape). **d**, Optical image of a metallic layered MoO_2 flake obtained at a high flow rate of oxygen. Scale bars, 10 µm (**a**–**d**). **e**, Ternary phase diagram of MoS_2, indicating the possible reaction routes for CVD growth of MoS_2. The star symbols represent the products obtained in this work. **f**, A TEM image of O-MoS_2. **g**, A selected-area electron diffraction pattern of the monolayer O-MoS_2 film. The sixfold-symmetric diffraction points correspond to the hexagonal lattice structure of monolayer MoS_2, indicating the highly crystalline nature of the as-grown crystals. **h**,**i**, XPS data of Mo 3*d* (**h**) and O 1s (**i**) for a typical CVD MoS_2 film grown under the sulfur-mild condition and an O-MoS_2 film, showing the presence of Mo–O bonds in O-MoS_2. The dashed lines highlight the shift in binding energies. The redshifted binding energies in the O-MoS_2 film indicate the less n-type doping in O-MoS_2. The weak intensity of Mo–O peaks in a typical CVD MoS_2 film is likely to be associated with the physisorption of oxygen in the environment[30] or MoO_x clusters deposited onto the substrate during the growth.

are observed, which is consistent with previously reports results[10]. In contrast, this unintentional n-type doping is substantially suppressed in the O-MoS_2 sample. This observation is also consistent with the trend found in the PL spectra. A detailed discussion on the strain distributions in these three types of as-grown MoS_2 crystal and its effects on PL are provided in Supplementary Section 4.

DFT calculations are performed to understand the effects of V_S and oxygen dopants on the monolayer MoS_2 samples. Figure 3 shows the atomic structures and local density of states (LDOS) of defective and oxygen-incorporated monolayer MoS_2. Compared with perfect monolayer MoS_2 (Fig. 3a), the presence of V_S introduces donor defect states within the bandgap of MoS_2 (Fig. 3b). These states increase the electron concentrations and decrease the work function of MoS_2 (Supplementary Fig. 11a). On the other hand, when the V_S sites are bound to one or two oxygen atoms, such donor defect states are eliminated, giving rise to the depletion of electrons and an increased work function in O-MoS_2 (Fig. 3c,d and Supplementary Fig. 11b). This theoretical observation agrees with previous experimental results[52] and can explain the electron depletion effect discussed above, as well as the transport properties of O-MoS_2 transistors (discussed later). There are additional features in the DFT calculation results that are related to the low-temperature spectroscopic characteristics induced by oxygen passivation, which will also be discussed later.

Improved performance of monolayer O-MoS_2 transistors

The removal of the donor state in O-MoS_2 crystals can greatly alter the device performance. We fabricate field-effect transistors (FETs) based on three types of MoS_2 sample (Fig. 4a) and characterize the transport properties. The electrical characterization of transistors is conducted in a high-vacuum environment (~10^{-6} torr) to avert other extrinsic doping effects induced by air or moisture. As evident in Fig. 4b, a clear shift in the threshold voltage (V_T) is observed in the O-MoS_2 FET with respect to the other two samples, which suggests lighter n-type doping in the O-MoS_2 channel. A statistical analysis of V_T shifts and field-effect mobilities (μ) for these three types of MoS_2 FET is shown in Fig. 4b, inset, and Supplementary Fig. 15. The V_T values for the SE-MoS_2 and SM-MoS_2 transistors lie in -17.0 ± 9.7 V and 2.8 ± 4.9 V, respectively, whereas the transistors based on the electron-depleted O-MoS_2 monolayers exhibit a 'normally

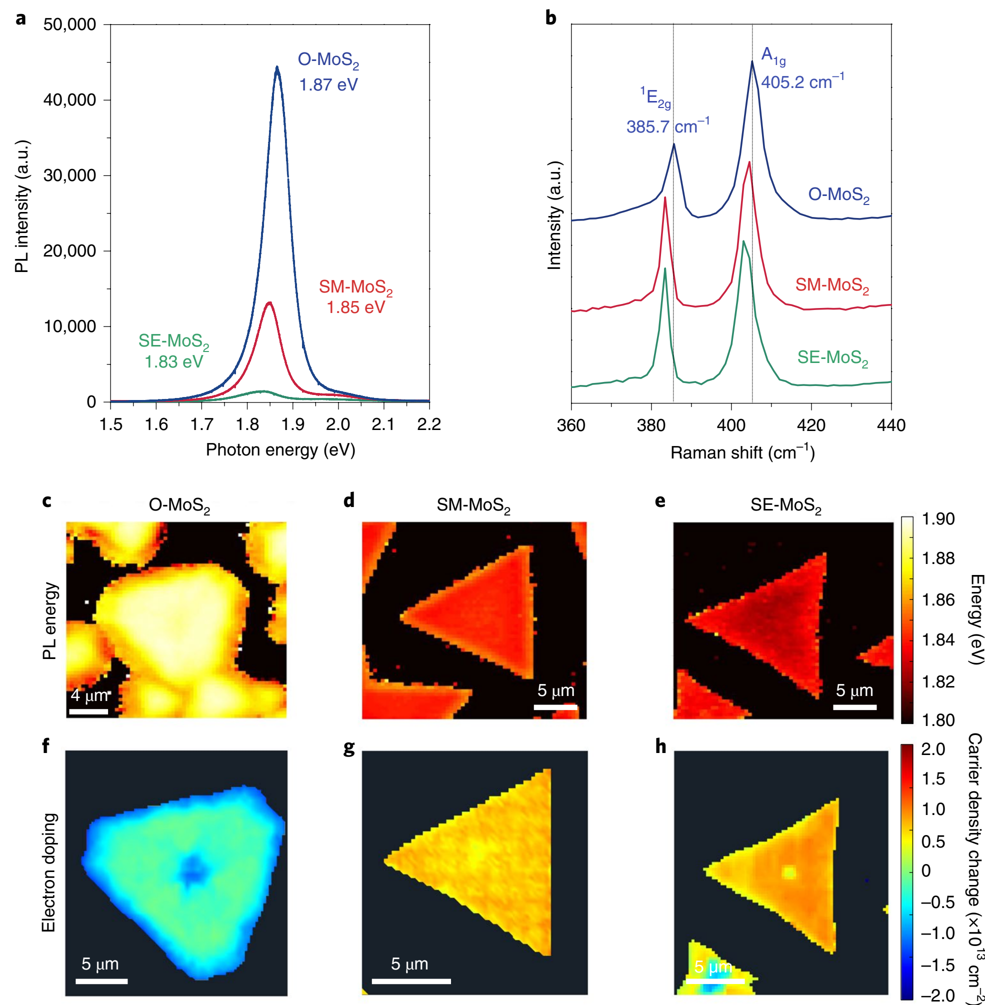

Fig. 2 | Reduction in electron doping of monolayer O-MoS_2. **a**, Typical PL spectra of O-MoS_2, SM-MoS_2 and SE-MoS_2 flakes grown on SiO_2/Si substrates acquired in an ambient environment, showing PL enhancement of O-MoS_2. **b**, Typical Raman spectra taken from these three types of MoS_2 monolayer. The blueshift in A_{1g} for O-MoS_2 suggests lower electron doping. **c–e**, Mapping of PL energy for the three types of MoS_2 flake. The electron-depleted domain of O-MoS_2 (**c**) shows a PL peak energy close to the neutral excitonic transition. In contrast, SM-MoS_2 (**d**) and SE-MoS_2 (**e**) crystals grown without oxygen display lower PL energies, corresponding to charged exciton (trion) transition. **f–h**, Mapping of the change in carrier densities extracted from the A_{1g} shifts for O-MoS_2 (**f**), SM-MoS_2 (**g**) and SE-MoS_2 (**h**). A significant reduction in electron doping is observed in O-MoS_2.

off' characteristic with a positive V_T of 21.0 ± 4.6 V. The V_T difference among these three types of transistor can be attributed to the Fermi-level shift in the MoS_2 channels, which are in accordance with the doping concentration difference observed in the PL and Raman measurements and the work-function shifts from DFT calculations. No mobility degradation is observed in the O-MoS_2 samples. The electrical characteristics and PL spectra of O-MoS_2 are consistent in both vacuum and air (Supplementary Figs. 25 and 26), suggesting the stable chemical bonding, rather than physisorption, of the oxygen dopants to the MoS_2 lattice.

The work functions of monolayer MoS_2 FET channels with and without oxygen incorporation are experimentally characterized via EFM. The insets in Fig. 4c show the scans of the EFM phase of MoS_2 (top-left inset) relative to the grounded Au electrode (bottom-right inset) for the same tip voltage. The striking phase contrast difference between O-MoS_2 (top) and SM-MoS_2 (bottom) suggests a difference in their electrical properties, and their work functions extracted from a series of EFM scans at different tip voltages are shown in Fig. 4c (Supplementary Fig. 9b). More details about the extraction of work function from EFM is provided in Supplementary Section 6. Figure 4c demonstrates that O-MoS_2 indeed exhibits a higher work function than SM-MoS_2. This increase in work function with oxygen incorporation is consistent with experimental observations from PL, Raman and electrical characterization. Taking the work function of Au electrodes as the reference (5.2 eV)[22], O-MoS_2 has a work function of 5.45 ± 0.05 eV, which is higher than the reported values for MoS_2 treated with physically absorbed oxygen and plasma-treated MoS_2 (ref. [34,53]). This work function is also distinct from that of SM-MoS_2, which is 5.19 ± 0.05 eV. These results are in good agreement with the DFT calculations (Fig. 4c and Supplementary Fig. 11).

The incorporation of oxygen into monolayer O-MoS_2 also reduces the contact resistance of MoS_2 devices. Figure 4d and Supplementary Fig. 12 show the room-temperature output characteristics (I_{DS}–V_{DS}) of three types of monolayer MoS_2 transistor with Ni contacts. The O-MoS_2 FETs exhibit ohmic-like characteristics at room temperature, whereas the SM-MoS_2 and SE-MoS_2 transistors show nonlinear, Schottky characteristics. This linear I_{DS}–V_{DS} response for the O-MoS_2 transistors suggests that the energy barrier at the Ni/O-MoS_2 interface is relatively small. To investigate the energy barrier at the contact interface, the thermionic emission model is applied to extract the Schottky barriers at the

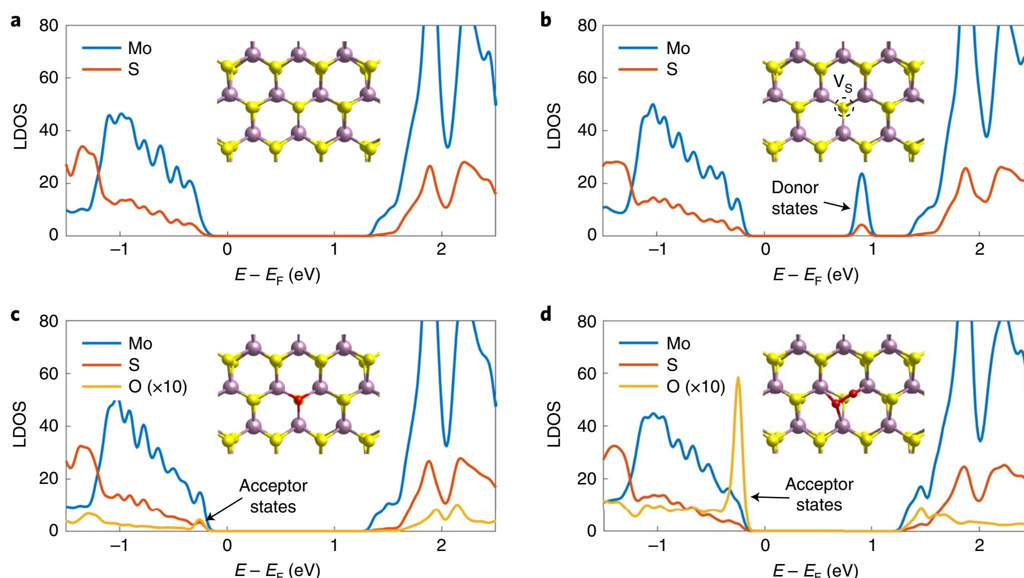

Fig. 3 | Atomic structures and DFT calculation results of the effect of oxygen healing. **a**, LDOS as a function of the electron energy (E) relative to the Fermi level E_F of pristine monolayer MoS_2. Inset: atomic structure of monolayer MoS_2 (purple, molybdenum atoms; yellow, sulfur atoms). **b**, LDOS of defective monolayer MoS_2 possessing V_S. Donor-like states emerge below the conduction band edge. The V_S site is highlighted by the dashed circle shown in the inset. **c**,**d**, LDOS of monolayer MoS_2 with a single oxygen atom (red atom in the inset) (**c**) and two oxygen atoms (red atoms in the inset) (**d**) bonded to the V_S sites. The presence of oxygen dopants heals the V_S-induced donor defect states and introduces additional acceptor-like states near the valence band edges. Insets, corresponding atomic structures obtained from the DFT calculations.

Ni/MoS_2 junction (Supplementary Section 10). Supplementary Fig. 17 shows the extracted effective energy barriers at various gate voltages for these three types of transistor. The SBH in the O-MoS_2 FET at the flat-band condition is extracted to be 40 meV (Supplementary Fig. 17d), which are much lower than those extracted from both SE-MoS_2 and SM-MoS_2 devices (namely, 100 and 200 meV, respectively; Supplementary Fig. 17e,f). Such a low contact barrier is confirmed in several O-MoS_2 FETs (Supplementary Fig. 18). Note that the SBH observed in O-MoS_2 FET is also smaller than those characterized from different types of contact to MoS_2 devices in previous reports (100–400 meV)[22–27]. For a high-SBH device such as SE-MoS_2 and SM-MoS_2 FETs, the drain current (I_{DS}) significantly drops with decreasing temperature, which is due to the reduced thermionic emission current across the Schottky barrier (Supplementary Fig. 14b,c). We note that I_{DS} in the O-MoS_2 FET shows lower sensitivity to the decrease in temperature (Supplementary Fig. 14a), reflecting the nature of the lower energy barrier at the contact interface, although its I_{DS}–V_{DS} curves still turn to nonlinear characteristics at a low temperature due to the presence of the small Schottky barrier (Supplementary Fig. 13).

Given that SBH is supposed to be equal to the energy difference between the work function of the metal contact and the electron affinity of the semiconductor in an ideal case (Schottky–Mott limit), such inconsistency in SBHs for these three types of FET implies the presence of different extents of Fermi-level pinning at the Ni/MoS_2 interfaces (Fig. 4g–j). There are two possible origins of Fermi-level pinning: pinning by metal-induced gap states (MIGS)[54], in which the electron wave functions of the metal 'leak' into the semiconductor at the interface, resulting in a broad continuum of states in the bandgap of the semiconductor, and giving rise to Fermi-level pinning somewhere within the bandgap; in defect-state pinning, the Fermi level is pinned at the energy level with the highest density of defect states[55,56]. Neither of these two pinning mechanisms is necessarily correlated with the energy difference between the metal work function and electron affinity of the semiconductor. Generally speaking, these two pinning mechanisms compete at the metal/semiconductor interface, and the Fermi level is fixed at the overall charge neutrality level. Given the abundant V_S states below the CBM in SM- or SE-MoS_2, and the absence of any deep donor states in O-MoS_2 as predicted by the DFT calculation results (Fig. 3 and Supplementary Fig. 10), we believe that the SBHs in SM- or SE-MoS_2 and in O-MoS_2 are dominated by defect-state pinning and MIGS pinning, respectively, in which the Fermi level determined by MIGS may be closer to the CBM of MoS_2, allowing for a lower SBH.

The R_C value for a semiconductor device is determined by the SBH at the interface. We extract the R_C value of the three types of MoS_2 FET through the transfer length method[26,57]. As expected, SM-MoS_2 and SE-MoS_2 FETs exhibit high R_C of around 3.9 and 7.8 kΩ μm, respectively, due to their high SBHs (Fig. 4e and Supplementary Fig. 19b). Compared with typical CVD MoS_2 grown without oxygen, the low SBH of the O-MoS_2 transistor yields a lower R_C value of ~1 kΩ μm at the same carrier density (n_{2D}) of 4×10^{12} cm^{-2} (Fig. 4e and Supplementary Fig. 19b,c). Figure 4e summarizes the resulting SBH and R_C for the three types of monolayer MoS_2 FET. It is worth mentioning that the improved R_C value for the O-MoS_2 FETs is also lower than previously reported Ni[57,58], van der Waals and interlayer contacts ($R_C \approx 3$ kΩ μm)[26,59], as summarized in Fig. 4f.

The monolayer O-MoS_2 FETs exhibit an average field-effect electron mobility of ~15 cm^2 V^{-1} s^{-1} (Fig. 4b, inset), comparable to those in typical CVD MoS_2 in this work and in previous studies[38,41]. This suggests that oxygen incorporation in MoS_2 lattices does not lead to severe mobility degradation caused by either dopant scattering or changes in carrier effective mass (that is, the curvature of CBM of O-MoS_2 is nearly unchanged; Supplementary Fig. 10). It is worth mentioning that although O-MoS_2 monolayers possess an increased work function, the devices still show n-type conduction. This is because Ni contacts used in this study still yield a lower SBH for electron injection (Fig. 4g,i), but rather higher SBH for holes, even after oxygen passivation. One should note that to realize high-performance p-type MoS_2 FETs, two factors must be simultaneously satisfied: first, a channel with a high work function; second, a low SBH at the metal/MoS_2 interface for hole injection. Our results

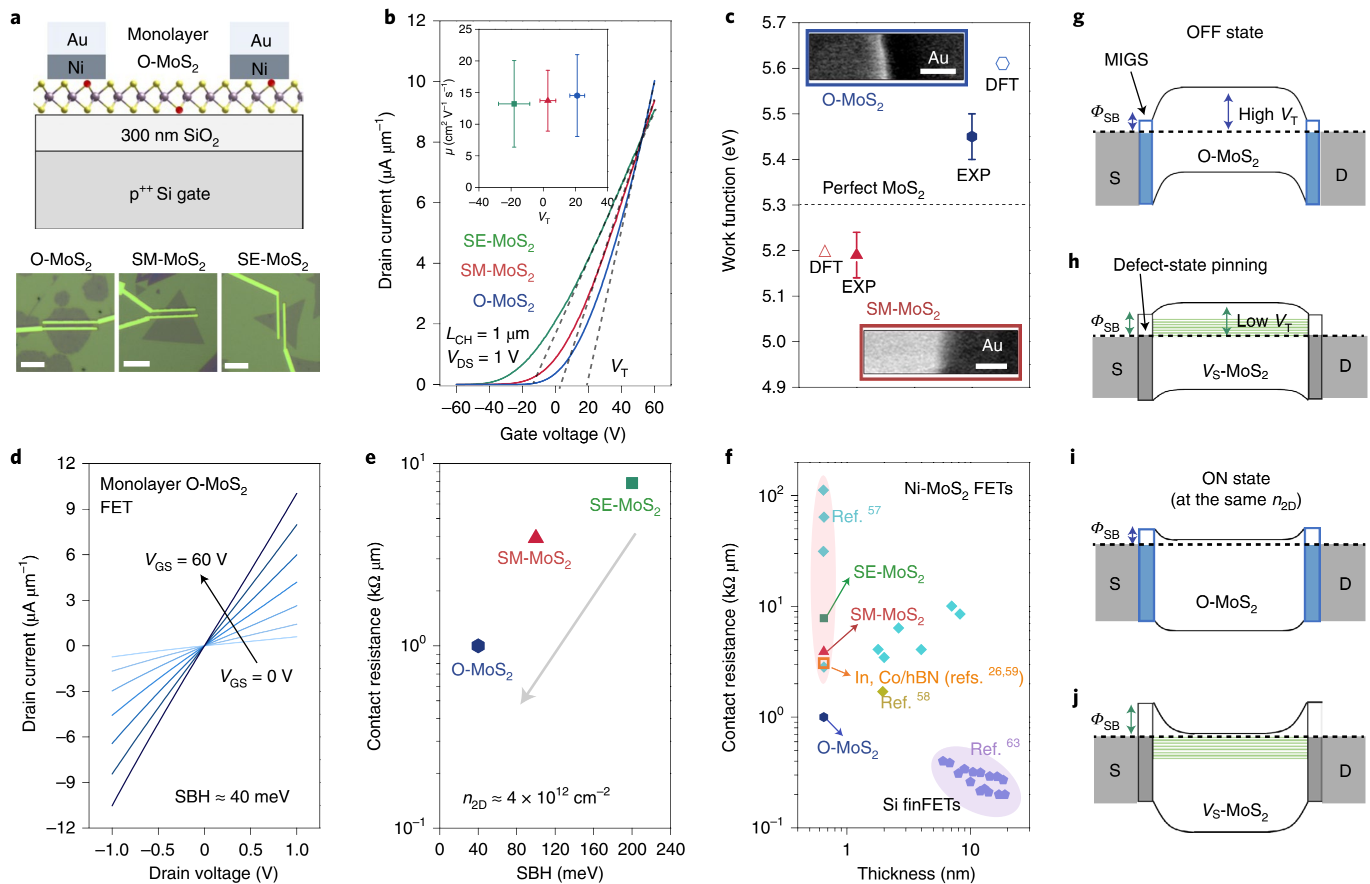

Fig. 4 | Electrical characterization of monolayer O-MoS$_2$ FETs. a, Schematic and the corresponding optical images of as-fabricated FETs with monolayer O-MoS$_2$, SM-MoS$_2$ and SE-MoS$_2$. The channel length (L_{CH}) is 1 µm. Scale bars, 10 µm. **b**, Transfer characteristics (drain current I_{DS} versus gate voltage V_{GS}) at a drain–source voltage (V_{DS}) of 1 V at room temperature. Inset: means and standard deviations of V_T and field-effect mobility (μ) extracted from the measurements of 80 FETs. **c**, Work functions (means and standard deviations) of MoS$_2$ FET channels with and without oxygen incorporation directly measured via EFM (EXP) in a nitrogen environment, as well as those calculated from DFT. Insets: the EFM phase of the monolayer MoS$_2$ (left) channel relative to the grounded Au electrode (right) for the same tip voltage (red, SM-MoS$_2$; blue, O-MoS$_2$; scale bars, 100 nm). The filled hexagon (filled and open triangles) represent the work functions of O-MoS$_2$ (SM-MoS$_2$) acquired from experimental EFM and theoretical DFT, respectively. **d**, Output characteristics (I_{DS} versus drain voltage V_{DS}) of a monolayer O-MoS$_2$ transistor. **e**, R_C versus SBH. The R_C values are extracted at n_{2D} of 4×10^{12} cm^{-2}. **f**, R_C versus thickness of MoS$_2$ transistors with Ni contacts (light blue and yellow) and van der Waals contacts (orange) and one example of Si fin field-effect transistors (finFETs; purple) from the literature[26,57–59,63]. The O-MoS$_2$ monolayers exhibit an improved R_C for Ni-contacted MoS$_2$ FETs. **g**,**h**, Band diagrams for the OFF states of 2D FETs fabricated on O-MoS$_2$ (**g**) and MoS$_2$ with donor defect states (**h**) (V_S-MoS$_2$ representing both SE-MoS$_2$ and SM-MoS$_2$). S, source; D, drain. Φ_{SB}, Schottky barrier height. The larger work function (namely, the lower Fermi level) of the O-MoS$_2$ channel gives rise to a positive shift of V_T. The MIGS induced at the Ni/MoS$_2$ interfaces are qualitatively illustrated in blue. The presence of the deep donor states (illustrated in green) in defective MoS$_2$ leads to defect-state pinning at the interface, resulting in a higher SBH. **i**,**j**, Band diagrams for the ON states of the 2D FETs fabricated on O-MoS$_2$ (**i**) and defective MoS$_2$ (**j**) at the same carrier density of the 2D channel, indicating a lower SBH in O-MoS$_2$ FETs.

illustrate the feasibility of enlarging the work function and eliminating the defect-state pinning of the MoS$_2$ channel through a one-step CVD process. Further investigation on various metal contacts to monolayer O-MoS$_2$ would be a promising direction for the development of p-type monolayer MoS$_2$ FETs.

Defect-state-bound excitons in monolayer MoS$_2$

To further investigate the evolution of defect states induced by the proposed oxygen-incorporated defect-healing process, PL spectroscopy measurements are carried out at low temperature. The temperature-dependent PL measurements for the three types of MoS$_2$ sample are summarized in Supplementary Fig. 22, and the temperature dependence of the observed free-exciton emissions is in accordance with previous studies[34,48]. At lower temperatures (<160 K), besides the free-exciton emissions located at around 1.95 eV, additional PL emission peaks emerge at lower photon energies (from 1.65 to 1.85 eV). These PL emission peaks have been widely observed in previous studies on MoS$_2$ produced by either mechanical exfoliation or CVD growth and treated with or without O$_2$ plasma[34,60]. Sublinear power dependence of these low-energy PL emission peaks at 77 K is observed (Supplementary Fig. 23), which is in accordance with previous studies[34]. We, thus, attribute the low-energy PL emissions to the radiative recombination of excitons bound to localized defect states. By fitting the power dependent bound-exciton PL emissions with a power law, that is, $I_{PL} \approx P^{\alpha}$, where P is the incident light power, we notice that the power factor α for O-MoS$_2$ and SM-MoS$_2$ samples are 0.72 and 0.88, respectively (Supplementary Fig. 23c). Such a discrepancy in α suggests that the bound exciton states in O-MoS$_2$ and SM-MoS$_2$ may originate from different defect states.

To gather more information about the exciton states in MoS$_2$, we take gate-dependent PL measurements. The PL spectra of O-MoS$_2$,

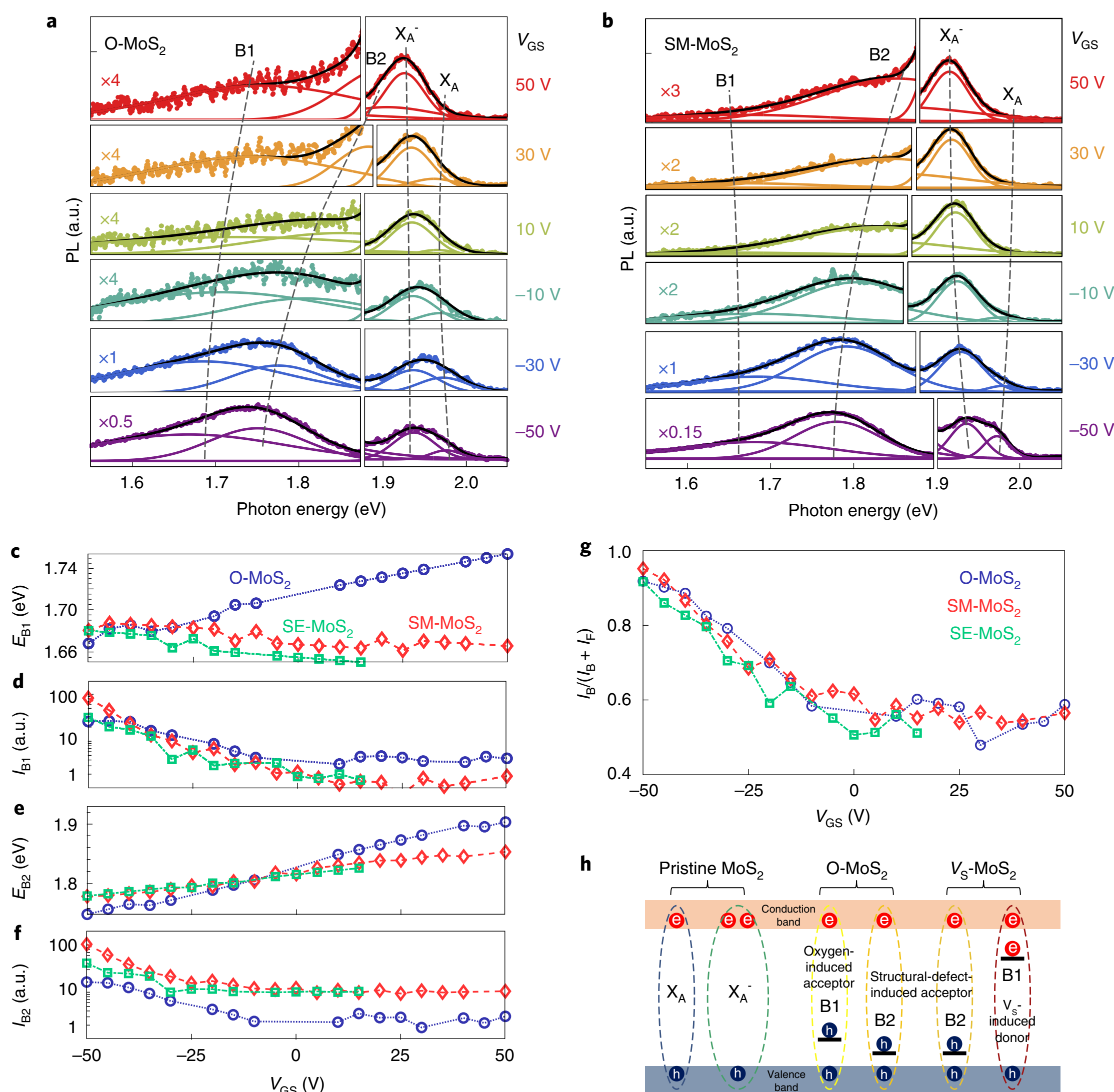

Fig. 5 | Gate-dependent PL at 78 K. a,**b**, PL spectra of O-MoS$_2$ (**a**) and SM-MoS$_2$ (**b**) at 78 K with different gate voltages (V_{GS}). Each spectrum is fitted with four Gaussian peaks, denoted as B1, B2, X_A and X_A^-. **c**–**f**, Peak positions E_{B1} (**c**) and E_{B2} (**e**) and accumulated intensities I_{B1} (**d**) and I_{B2} (**f**) of the B1 and B2 bound exciton states as a function of V_{GS}. The parameters for O-MoS$_2$, SM-MoS$_2$ and SE-MoS$_2$ are plotted as blue circles, red diamonds and green squares, respectively. **g**, Percentage of bound-exciton-associated accumulative PL intensity ($I_B/(I_B+I_F)$) as a function of V_{GS}. **h**, Diagram of free and bound excitons probed in monolayer MoS$_2$. e, electron; h, hole.

SM-MoS$_2$ and SE-MoS$_2$ with different gate voltages (V_{GS}) are shown in Fig. 5a,b and Supplementary Fig. 24a–c. The free-exciton PL emission at higher photon energies (from 1.85 to 2.00 eV) can be fitted with two Gaussian functions, denoted as X_A^- and X_A. The bound-exciton PL emission at lower energies (from 1.65 to 1.85 eV) can be fit with two additional Gaussian functions, denoted as B1 and B2. The gate-dependent peak energies and peak intensities for the negatively charged excitons (or trions, X_A^-) and neutral excitons (X_A) for the three different types of MoS$_2$ sample are plotted in Supplementary Fig. 24d–h, which are in good agreement with previous studies. More importantly, it is also observed that both peak energies and peak intensities of the B1 and B2 bound exciton emissions vary with gate voltage (Fig. 5c–f).

The trends in exciton peak energy and intensity can be summarized for the three flake types. The peak intensities of both B1 and B2 bound exciton emissions decrease with increasing V_{GS} for all three types of MoS$_2$ samples. This trend is more evident if we plot $I_B/(I_B+I_F)$ as a function of V_{GS} (Fig. 5g), where I_B and I_F are the accumulated PL intensities for bound excitons (B1 and B2) and free excitons (X_A^- and X_A), respectively. The intensity drop can be understood by considering the free-carrier screening of the charged impurity in MoS$_2$. The probability of bound exciton formation is determined by the Debye length of ionized impurity scattering[61] that is screened by the carriers in MoS$_2$, given by $L_D=(\kappa_s\varepsilon_0 k_B T/q^2 n_{2D})^{1/2}$, where κ_s is the relative permittivity, ε_0 is the vacuum permittivity, k_B is the Boltzmann constant, T is the temperature and q is the elementary charge. Evidently, L_D is negatively correlated with electron density due to screening of the Coulomb potential around the charged impurity, which, in turn, influences the population of bound excitons.

The peak energies of B1 and B2 emissions are also tuned by V_{GS}. Specifically, when the gate voltage increases, there is a redshift in the B1 peak in the SM- and SE-MoS$_2$ samples, whereas the B1 peak in the O-MoS$_2$ sample undergoes a blueshift. Meanwhile, a blueshift is observed in the B2 peak in all the three types of sample. These shifts in peak positions can be explained by the exciton recoil effects[15,48,62]. For a charged exciton (defect-bound exciton), since there is an additional electron or hole, the dissociation of these quasiparticles must

accompany an emission of this extra carrier, which consumes extra energy depending on the Fermi level. The directions of shifts in the peak position are opposite for a negatively charged exciton (donor bound) and for a positively charged exciton (acceptor bound). We, thus, identify the B1 state in the O-MoS_2 sample and the B2 state in all the three types of sample as acceptor-bound exciton states; further, the B1 state in the SM- and SE-MoS_2 samples is a donor-bound exciton state. The disappearance of the donor-bound exciton state and the emergence of a new acceptor state happen simultaneously as oxygen is incorporated into the MoS_2 lattices (Fig. 5h).

The LDOS values have shown that the presence of V_S generates defect states below the CBM of MoS_2 (Fig. 3b), whereas they are successfully eliminated in O-MoS_2 (Fig. 3c,d). Accordingly, these defect states can be associated with the donor-bound exciton state that is only observed in the SM-MoS_2 and SE-MoS_2 samples. On the other hand, the absence of the donor-bound exciton state in O-MoS_2 again evidences that such donor defect states have been effectively healed. Note that both defective and oxygen-incorporated MoS_2 exhibit native acceptor-like states close to the valence band minimum (VBM) (Fig. 3b–d and Supplementary Fig. 10), which may be the origin of the B2 acceptor-bound exciton state observed in all three types of MoS_2. Because the emergence of an additional acceptor-bound state (B1) takes place only in O-MoS_2, but not in SM-MoS_2 or SE-MoS_2, we speculate that B1 is likely to be associated with the acceptor states that are partially contributed by the O orbitals near the VBM (Fig. 3d). Another important observation is that there are additional O-orbital-contributed states near both CBM and VBM. These shallow defect states behave like effective donors and acceptors, respectively, and thus are mostly complementary to each other. This may be the reason why only less n-type doping—rather than p-type doping—is achieved for O-MoS_2 samples, as shown in Fig. 4.

Conclusions

We have reported an O_2-CVD technique for fabricating monolayer MoS_2 that passivates V_S and suppresses the formation of detrimental donor states. Raman, PL and XPS measurements demonstrate the presence of Mo–O bonds and the resulting electron depletion effect in MoS_2. The as-grown O-MoS_2 crystals, in comparison to typical CVD MoS_2, exhibit a higher work function (5.45 eV) and enhanced PL intensity. Oxygen incorporation also lowers the SBH (<40 meV) and consequently results in a low R_C (1 kΩ μm) at the metal/semiconductor heterojunction. These features are desirable for the development of high-performance MoS_2 transistors through O_2-CVD and other defect engineering approaches. The defect-healing process based on a one-step CVD strategy could also potentially open a route to modulate the electronic and optoelectronic properties of other 2D TMDs, in an approach that should be scalable and compatible with complementary metal–oxide–semiconductor processes.

Data availability

The data that support the findings within this paper are available from the corresponding author upon reasonable request.

Received: 25 July 2020; Accepted: 8 November 2021;
Published online: 23 December 2021

References

1. Erwin, S. C. et al. Doping semiconductor nanocrystals. *Nature* **436**, 91–94 (2005).
2. Chen, B. et al. Highly emissive and color-tunable $CuInS_2$-based colloidal semiconductor nanocrystals: off-stoichiometry effects and improved electroluminescence performance. *Adv. Funct. Mater.* **22**, 2081–2088 (2012).
3. Nowotny, M. K., Sheppard, L. R., Bak, T. & Nowotny, J. Defect chemistry of titanium dioxide. Application of defect engineering in processing of TiO_2-based photocatalysts. *J. Phys. Chem. C* **112**, 5275–5300 (2008).
4. Ambacher, O. et al. Two-dimensional electron gases induced by spontaneous and piezoelectric polarization charges in N- and Ga-face AlGaN/GaN heterostructures. *J. Appl. Phys.* **85**, 3222–3233 (1999).
5. Chhowalla, M., Jena, D. & Zhang, H. Two-dimensional semiconductors for transistors. *Nat. Rev. Mater.* **1**, 16052 (2016).
6. Schmidt, H., Giustiniano, F. & Eda, G. Electronic transport properties of transition metal dichalcogenide field-effect devices: surface and interface effects. *Chem. Soc. Rev.* **44**, 7715–7736 (2015).
7. Schmidt, H. et al. Transport properties of monolayer MoS_2 grown by chemical vapor deposition. *Nano Lett.* **14**, 1909–1913 (2014).
8. Yuan, S., Roldán, R., Katsnelson, M. & Guinea, F. Effect of point defects on the optical and transport properties of MoS_2 and WS_2. *Phys. Rev. B* **90**, 041402 (2014).
9. Ge, Y., Wan, W., Feng, W., Xiao, D. & Yao, Y. Effect of doping and strain modulations on electron transport in monolayer MoS_2. *Phys. Rev. B* **90**, 035414 (2014).
10. Chae, W. H., Cain, J. D., Hanson, E. D., Murthy, A. A. & Dravid, V. P. Substrate-induced strain and charge doping in CVD-grown monolayer MoS_2. *Appl. Phys. Lett.* **111**, 143106 (2017).
11. Vancsó, P. et al. The intrinsic defect structure of exfoliated MoS_2 single layers revealed by scanning tunneling microscopy. *Sci. Rep.* **6**, 29726 (2016).
12. Zhou, W. et al. Intrinsic structural defects in monolayer molybdenum disulfide. *Nano Lett.* **13**, 2615–2622 (2013).
13. Hong, J. et al. Exploring atomic defects in molybdenum disulphide monolayers. *Nat. Commun.* **6**, 6293 (2015).
14. Guo, Y., Liu, D. & Robertson, J. Chalcogen vacancies in monolayer transition metal dichalcogenides and Fermi level pinning at contacts. *Appl. Phys. Lett.* **106**, 173106 (2015).
15. Shang, J. et al. Revealing electronic nature of broad bound exciton bands in two-dimensional semiconducting WS_2 and MoS_2. *Phys. Rev. Mater.* **1**, 074001 (2017).
16. Amani, M. et al. Near-unity photoluminescence quantum yield in MoS_2. *Science* **350**, 1065–1068 (2015).
17. Lien, D.-H. et al. Electrical suppression of all nonradiative recombination pathways in monolayer semiconductors. *Science* **364**, 468–471 (2019).
18. Cho, K. et al. Electrical and optical characterization of MoS_2 with sulfur vacancy passivation by treatment with alkanethiol molecules. *ACS Nano* **9**, 8044–8053 (2015).
19. Mouri, S., Miyauchi, Y. & Matsuda, K. Tunable photoluminescence of monolayer MoS_2 via chemical doping. *Nano Lett.* **13**, 5944–5948 (2013).
20. McDonnell, S., Addou, R., Buie, C., Wallace, R. M. & Hinkle, C. L. Defect-dominated doping and contact resistance in MoS_2. *ACS Nano* **8**, 2880–2888 (2014).
21. Schulman, D. S., Arnold, A. J. & Das, S. Contact engineering for 2D materials and devices. *Chem. Soc. Rev.* **47**, 3037–3058 (2018).
22. Kim, C. et al. Fermi level pinning at electrical metal contacts of monolayer molybdenum dichalcogenides. *ACS Nano* **11**, 1588–1596 (2017).
23. Kim, G.-S. et al. Schottky barrier height engineering for electrical contacts of multilayered MoS_2 transistors with reduction of metal-induced gap states. *ACS Nano* **12**, 6292–6300 (2018).
24. Wang, J. et al. High mobility MoS_2 transistor with low Schottky barrier contact by using atomic thick h-BN as a tunneling layer. *Adv. Mater.* **28**, 8302–8308 (2016).
25. Liu, Y. et al. Approaching the Schottky–Mott limit in van der Waals metal–semiconductor junctions. *Nature* **557**, 696–700 (2018).
26. Wang, Y. et al. Van der Waals contacts between three-dimensional metals and two-dimensional semiconductors. *Nature* **568**, 70–74 (2019).
27. Chee, S. S. et al. Lowering the Schottky barrier height by graphene/Ag electrodes for high-mobility MoS_2 field-effect transistors. *Adv. Mater.* **31**, 1804422 (2019).
28. Yu, Z. et al. Towards intrinsic charge transport in monolayer molybdenum disulfide by defect and interface engineering. *Nat. Commun.* **5**, 5290 (2014).
29. Tongay, S. et al. Broad-range modulation of light emission in two-dimensional semiconductors by molecular physisorption gating. *Nano Lett.* **13**, 2831–2836 (2013).
30. Nan, H. et al. Strong photoluminescence enhancement of MoS_2 through defect engineering and oxygen bonding. *ACS Nano* **8**, 5738–5745 (2014).
31. Leong, W. S. et al. Tuning the threshold voltage of MoS_2 field-effect transistors via surface treatment. *Nanoscale* **7**, 10823–10831 (2015).
32. Lu, J. et al. Atomic healing of defects in transition metal dichalcogenides. *Nano Lett.* **15**, 3524–3532 (2015).
33. Islam, M. R. et al. Tuning the electrical property via defect engineering of single layer MoS_2 by oxygen plasma. *Nanoscale* **6**, 10033–10039 (2014).
34. Tongay, S. et al. Defects activated photoluminescence in two-dimensional semiconductors: interplay between bound, charged and free excitons. *Sci. Rep* **3**, 2657 (2013).
35. Kim, M. S. et al. Photoluminescence wavelength variation of monolayer MoS_2 by oxygen plasma treatment. *Thin Solid Films* **590**, 318–323 (2015).

36. Ling, X. et al. Role of the seeding promoter in MoS_2 growth by chemical vapor deposition. *Nano Lett.* **14**, 464–472 (2014).
37. Wang, S. et al. Shape evolution of monolayer MoS_2 crystals grown by chemical vapor deposition. *Chem. Mater.* **26**, 6371–6379 (2014).
38. Dumcenco, D. et al. Large-area epitaxial monolayer MoS_2. *ACS Nano* **9**, 4611–4620 (2015).
39. Van Der Zande, A. M. et al. Grains and grain boundaries in highly crystalline monolayer molybdenum disulphide. *Nat. Mater.* **12**, 554–561 (2013).
40. Liu, Z. et al. Strain and structure heterogeneity in MoS_2 atomic layers grown by chemical vapour deposition. *Nat. Commun.* **5**, 5246 (2014).
41. Smithe, K. K., English, C. D., Suryavanshi, S. V. & Pop, E. Intrinsic electrical transport and performance projections of synthetic monolayer MoS_2 devices. *2D Mater.* **4**, 011009 (2016).
42. Chen, W. et al. Oxygen-assisted chemical vapor deposition growth of large single-crystal and high-quality monolayer MoS_2. *J. Am. Chem. Soc.* **137**, 15632–15635 (2015).
43. Cao, D., Shen, T., Liang, P., Chen, X. & Shu, H. Role of chemical potential in flake shape and edge properties of monolayer MoS_2. *J. Phys. Chem. C* **119**, 4294–4301 (2015).
44. Gao, Y., Goodman, A. J., Shen, P.-C., Kong, J. & Tisdale, W. A. Phase-modulated degenerate parametric amplification microscopy. *Nano Lett.* **18**, 5001–5006 (2018).
45. Ponce-Mosso, M. et al. Enhanced photocatalytic activity of amorphous MoO_3 thin films deposited by rf reactive magnetron sputtering. *Catal. Today* **349**, 150–158 (2018).
46. Khademi, A., Azimirad, R., Zavarian, A. A. & Moshfegh, A. Z. Growth and field emission study of molybdenum oxide nanostars. *J. Phys. Chem. C* **113**, 19298–19304 (2009).
47. Diaz, H. C., Addou, R. & Batzill, M. Interface properties of CVD grown graphene transferred onto MoS_2(0001). *Nanoscale* **6**, 1071–1078 (2014).
48. Mak, K. F. et al. Tightly bound trions in monolayer MoS_2. *Nat. Mater.* **12**, 207–211 (2013).
49. Michail, A., Delikoukos, N., Parthenios, J., Galiotis, C. & Papagelis, K. Optical detection of strain and doping inhomogeneities in single layer MoS_2. *Appl. Phys. Lett.* **108**, 173102 (2016).
50. Rice, C. et al. Raman-scattering measurements and first-principles calculations of strain-induced phonon shifts in monolayer MoS_2. *Phys. Rev. B* **87**, 081307 (2013).
51. Chakraborty, B. et al. Symmetry-dependent phonon renormalization in monolayer MoS_2 transistor. *Phys. Rev. B* **85**, 161403 (2012).
52. Kim, J. H. et al. Work function variation of MoS_2 atomic layers grown with chemical vapor deposition: the effects of thickness and the adsorption of water/oxygen molecules. *Appl. Phys. Lett.* **106**, 251606 (2015).
53. Lee, S. Y. et al. Large work function modulation of monolayer MoS_2 by ambient gases. *ACS Nano* **10**, 6100–6107 (2016).
54. Tung, R. T. The physics and chemistry of the Schottky barrier height. *Appl. Phys. Rev.* **1**, 011304 (2014).
55. Huang, L. et al. Role of defects in enhanced Fermi level pinning at interfaces between metals and transition metal dichalcogenides. *Phys. Rev. B* **96**, 205303 (2017).
56. Bampoulis, P. et al. Defect dominated charge transport and Fermi level pinning in MoS_2/metal contacts. *ACS Appl. Mater. Interfaces* **9**, 19278–19286 (2017).
57. English, C. D., Shine, G., Dorgan, V. E., Saraswat, K. C. & Pop, E. Improved contacts to MoS_2 transistors by ultra-high vacuum metal deposition. *Nano Lett.* **16**, 3824–3830 (2016).
58. Smets, Q. et al. Ultra-scaled MOCVD MoS_2 MOSFETs with 42nm contact pitch and 250µA/µm drain current. In *2019 IEEE International Electron Devices Meeting (IEDM)* 23.22.21–23.22.24 (IEEE, 2019).
59. Cui, X. et al. Low-temperature ohmic contact to monolayer MoS_2 by van der Waals bonded Co/h-BN electrodes. *Nano Lett* **17**, 4781–4786 (2017).
60. Goodman, A. J., Willard, A. P. & Tisdale, W. A. Exciton trapping is responsible for the long apparent lifetime in acid-treated MoS_2. *Phys. Rev. B* **96**, 121404 (2017).
61. Lundstrom, M. *Fundamentals of Carrier Transport* (Cambridge Univ. Press, 2009).
62. Zhang, Q. et al. Recoil effect and photoemission splitting of trions in monolayer MoS_2. *ACS Nano* **11**, 10808–10815 (2017).
63. van Dal, M. J. H. et al. Highly manufacturable finFETs with sub-10nm fin width and high aspect ratio fabricated with immersion lithography. In *2007 IEEE Symposium on VLSI Technology* 110–111 (IEEE, 2017).

Acknowledgements

P.-C.S., H.W. and J.K. acknowledge financial support from the Center for Energy Efficient Electronics Science (NSF award no. 0939514). P.-C.S., Y.L., A.-Y.L., J.-H.P., T.P. and J.K. acknowledge the US Army Research Office (ARO) through the Institute for Soldier Nanotechnologies at MIT, under cooperative agreement no. W911NF-18-2-0048. C.M. and K.E.A. acknowledge support of grant NSF-DMR 1708970. C.S., J.-H.P., X.J., T.P. and J.K. acknowledge support from the US ARO MURI project under grant no. W911NF-18-1-0432. J.L. acknowledges support by the Office of Naval Research MURI through grant no. N00014-17-1-2661. Y.G., Y.L., N.M. and J.K. acknowledge support by the US Department of Energy, Office of Science, Basic Energy Sciences, under award DE-SC0020042. X.W. and X.L. acknowledge support of the Semiconductor Research Corporation. This work was supported in part by the STC Center for Integrated Quantum Materials, NSF grant no. DMR-1231319. This work was performed in part at the Center for Nanoscale Systems (CNS)—a member of the National Nanotechnology Coordinated Infrastructure Network, which is supported by the National Science Foundation under NSF award no. 1541959. CNS is part of Harvard University.

Author contributions

P.-C.S., Y.L. and J.K. conceived and designed the experiments. P.-C.S. performed the MoS_2 growth and characterization supervised by J.K. P.-C.S. and Y.L. carried out the device fabrication and characterization supervised by T.P. Y.L., P.-C.S. and X.W. performed the low-temperature optical measurements supervised by X.L. C.M. carried out the EFM measurements and interpreted the data supervised by K.E.A. A.-Y.L. performed the doping and strain characterization and analysed the Raman and XPS data. C.S. performed the TEM measurement supervised by J.L. C.S. and X.J. conducted the DFT calculations supervised by J.L. and Y.W. H.W. performed the XPS measurement. N.M. conducted the second-harmonic generation study supervised by W.T. Y.G. and X.J. assisted with further O-MoS_2 synthesis. P.-C.S., Y.L. and J.K. co-wrote the paper. All the authors regularly discussed the results and commented on the manuscript.

Competing interests

The authors declare no competing interests.

Additional information

Supplementary information The online version contains supplementary material available at https://doi.org/10.1038/s41928-021-00685-8.

Correspondence and requests for materials should be addressed to Jing Kong.

Peer review information *Nature Electronics* thanks the anonymous reviewers for their contribution to the peer review of this work.

Reprints and permissions information is available at www.nature.com/reprints.

Publisher's note Springer Nature remains neutral with regard to jurisdictional claims in published maps and institutional affiliations.

© The Author(s), under exclusive licence to Springer Nature Limited 2021

nature portfolio

https://doi.org/10.1038/s41928-021-00685-8

Supplementary information

Healing of donor defect states in monolayer molybdenum disulfide using oxygen-incorporated chemical vapour deposition

In the format provided by the authors and unedited

nature portfolio

https://doi.org/10.1038/s41928-021-00685-8

Supplementary information

Healing of donor defect states in monolayer molybdenum disulfide using oxygen-incorporated chemical vapour deposition

In the format provided by the authors and unedited

Supplementary Information

Healing of donor defect states in monolayer molybdenum disulfide using oxygen-incorporated chemical vapor deposition

Pin-Chun Shen[1,8], Yuxuan Lin[1,8], Cong Su[2], Christina McGahan[3], Ang-Yu Lu[1], Xiang Ji[1], Xingzhi Wang[4], Haozhe Wang[1], Nannan Mao[1,6], Yunfan Guo[1], Ji-Hoon Park[1], Yan Wang[5], William Tisdale[6], Ju Li[2], Xi Ling[4,7], Katherine E. Aidala[3], Tomás Palacios[1], and Jing Kong[1*]

[1]Department of Electrical Engineering and Computer Science, Massachusetts Institute of Technology, Cambridge, MA, USA

[2]Department of Nuclear Science and Engineering, Massachusetts Institute of Technology, Cambridge, MA, USA

[3]Department of Physics, Mount Holyoke College, South Hadley, MA, USA

[4]Department of Chemistry, Boston University, Boston, MA, USA

[5]Institute of Microelectronics, Tsinghua University, Beijing, China

[6] Department of Chemical Engineering, Massachusetts Institute of Technology, Cambridge, MA, USA

[7]Division of Materials Science and Engineering, Boston University, Boston, MA 02215, USA

[8]These authors contributed equally to this work.

[*]e-mail: jingkong@mit.edu

This document includes:

1. Chemical vapor deposition of monolayer MoS_2 with oxygen incorporation

2. Second harmonic generation (SHG) characterization of monolayer MoS_2

3. Transmission electron microscope (TEM) of monolayer O-MoS_2

4. Raman spectroscopy for doping and strain characterization of monolayer MoS_2

5. X-ray photoelectron spectroscopy (XPS) measurement

6. Electrostatic force microscope (EFM) characterization of monolayer MoS_2

7. First-principles calculation

8. Monolayer MoS_2 FET fabrication and characterization

9. Threshold voltage and mobility extraction

10. Extraction of Schottky barrier height (SBH) through thermionic emission model

11. Extraction of contact resistance and mobility by transfer length method (TLM)

12. Optical characterization of defect states in monolayer MoS_2

13. Electrical and optical properties of O-MoS_2 measured in air and in vacuum

14. The effect of electron irradiation on O-MoS_2 in scanning transmission electron microscope (STEM)

1. Chemical vapor deposition of monolayer MoS_2 with oxygen incorporation

All these three types of monolayer MoS_2 crystals are deposited on 300 nm SiO_2/Si substrates through sulfurization of molybdenum trioxide (MoO_3) powder placed in the middle of the tube (Supplementary Fig. 1). Perylene-3,4,9,10-tetracarboxylic acid tetrapotassium (PTAS) molecules are employed as the seed to facilitate the MoS_2 growth. PTAS solutions are spin-coated onto two pieces of clean SiO_2/Si, serving as the seed reservoirs. A clean target growth substrate is suspended between these two PTAS seed reservoirs. All these three substrates are faced downward and placed on a crucible containing the MoO_3 precursor. In this way, the seed molecules can diffuse and deposit onto the target SiO_2 substrate during the growth. A separate crucible with sulfur (S) powders is put upstream, 14 cm away from the MoO_3 crucible, within a low-temperature zone. The growth recipe for the monolayer MoS_2 grown under the sulfur-mild (SM) condition (S:20 mg, MoO_3: 20 mg, O_2: 0sccm) is referred to as the baseline condition in this work. A sulfur-excess (SE) condition corresponds to the recipe of S:40 mg, MoO_3: 20 mg, and O_2: 0 sccm. To investigate the oxygen effects, O-MoS_2 was grown based on the baseline (sulfur-mild) condition with extra introduction of oxygen flow rate (0.2 sccm). Before the growth, the CVD system is purged using a 1000 sccm flow of argon (Ar) for 5 min. Then, a 20 sccm flow of Ar and an additional 0-1 sccm flow of O_2 are introduced into the system as the carrier and reaction gases, respectively, through two separate mass flow controllers. To start the MoS_2 deposition, the temperature is increased from room temperature to 625 °C with a ramp rate of 30 °C min^{-1}. The monolayer MoS_2 crystals are grown at 625 °C for 3 min at atmospheric pressure. The temperature of the S source is kept at ~180 °C during the growth. Finally, the system is naturally cooled down to room temperature. During the cooling process, a 1000 sccm Ar flow is maintained in the chamber to remove the reactants, preventing further unintentional reactions.

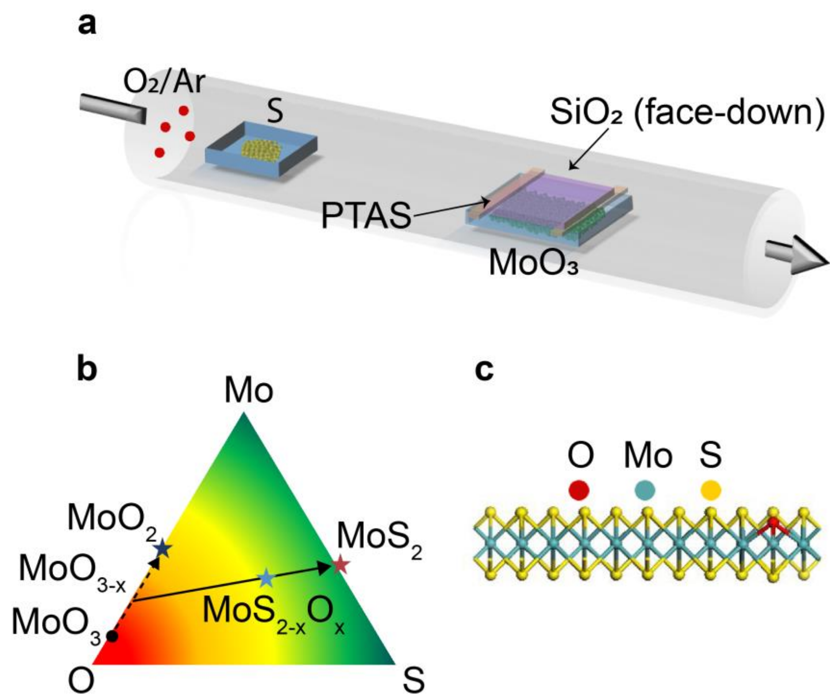

Supplementary Figure 1. a, Schematic illustration of the O_2-CVD system for the growth of monolayer O-MoS_2. **b,** Ternary phase diagram of MoS_2, indicating the possible reaction routes for CVD growth of MoS_2. The star symbols represent the products obtained in the work. **c,** The atomic structure of oxygen-doped MoS_2, showing that a sulfur atom is replaced by an oxygen atom.

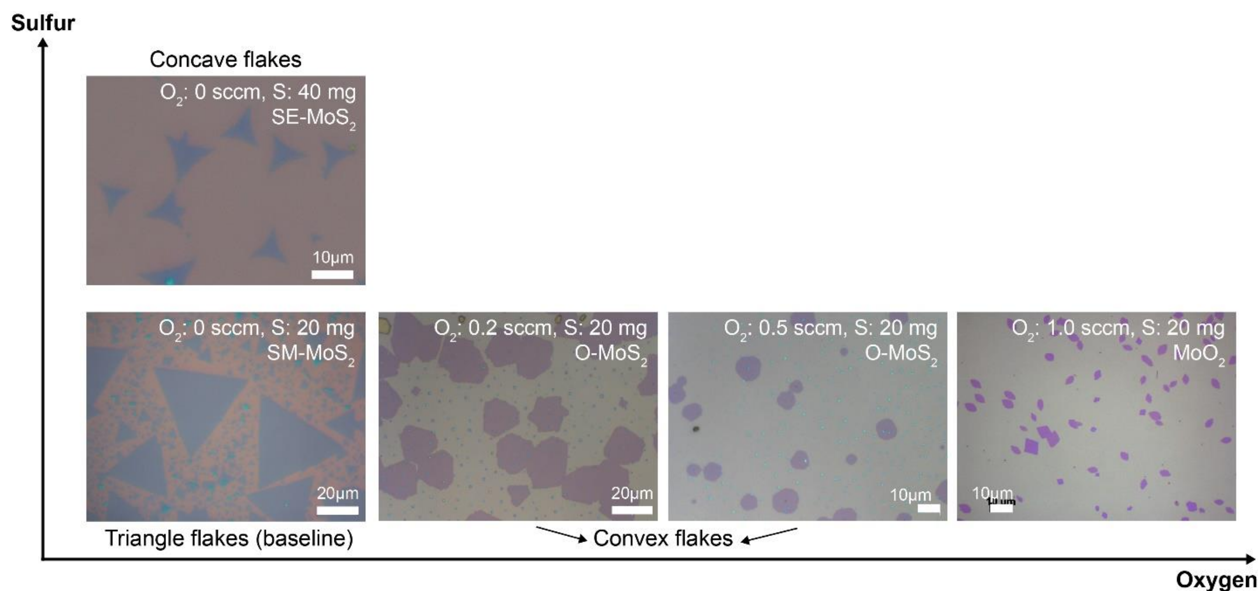

Supplementary Figure 2. Evolution of the MoS_2 crystal morphology with different growth conditions. The samples are grown using 20 mg of MoO_3 with various oxygen flow rates and sulfur amounts. A clear evolution of crystal shapes can be observed.

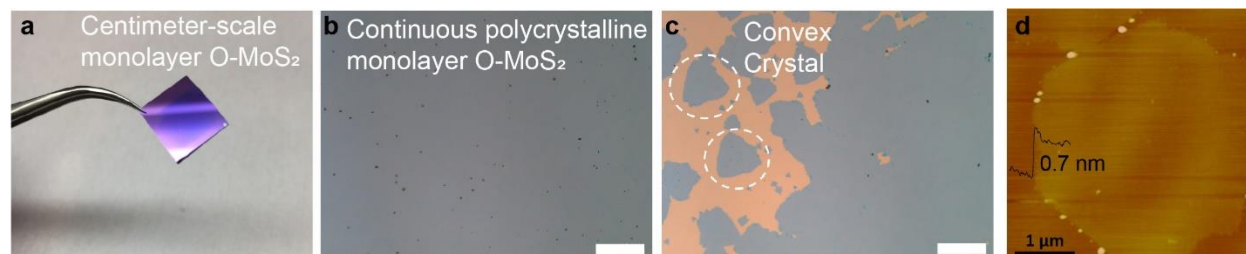

Supplementary Figure 3. a, Photograph of a centimeter-scale film of monolayer O-MoS_2 grown on a SiO_2/Si substrate. **b,** Optical image of the continuous polycrystalline monolayer O-MoS_2 film. Scale bar: 100 µm. **c,** Optical image of the edge of the film, showing individual convex O-MoS_2 flakes merging into a continuous film. Scale bar: 100 µm. **d,** Atomic force microscopic (AFM) image of a hexagonal O-MoS_2 flake. A thickness < 1 nm demonstrates its monolayer nature.

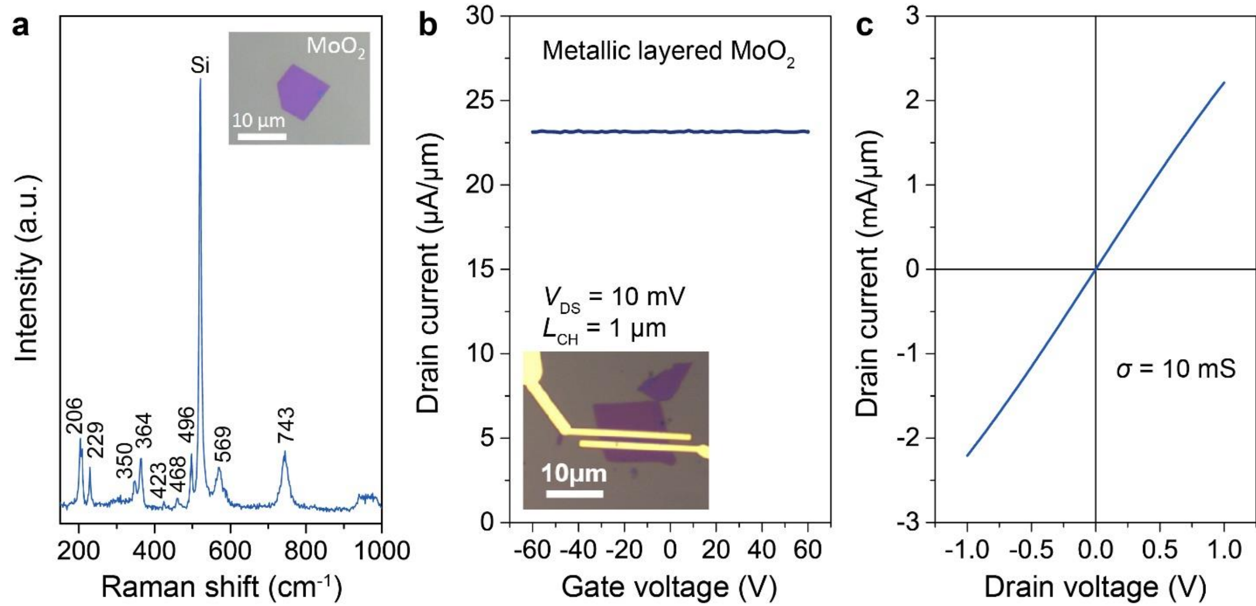

Supplementary Figure 4. Material characterization of CVD-grown layered MoO_2. **a,** The Raman spectrum of a layered MoO_2 flake grown on a 300-nm-thick SiO_2. The inset shows the optical microscopy image of a typical as-grown MoO_2 crystal. **b,** The transfer characteristic of a MoO_2 FET on a 300-nm-thick SiO_2 dielectric. The absence of gate dependence indicates the metallic nature of layered MoO_2. (Inset: optical microscopy image of the MoO_2 device) **c,** The output characteristic of the MoO_2 FET at zero gate bias.

2. Second harmonic generation (SHG) characterization of monolayer MoS_2

SHG experiments are performed in the reflection geometry on an inverted optical microscope (Nikon Ti-U). The fundamental light is supplied by a mode-locked Ti: sapphire oscillator (Coherent Mira HP) operating at a repetition rate of 76 MHz. The pulses are of 90 fs duration and centered at a wavelength of 830 nm. The excitation laser is focused by a 40X objective lens (Nikon, CFI S Plan Fluor ELWD, NA=0.6) onto the sample. The back-scattered SHG signals are collected by the same objective lens and reflected by a 50:50 beam splitter to a photon multiplier tube (R4220P). The residual 830nm fundamental light is removed by a short pass filter (Thorlabs, FES0450), a band pass filter (Semrock, FF01-440/SP-25) and a color glass filter (Thorlabs, FGB39). The 415nm SHG photons are counted by a single photon counter (Stanford Research System, SR400) in a gated mode. The polarized SHG mapping is performed by scanning the

samples on a piezo stage (P-545.xR8S PI nano XY Piezo System, Physikinstrumente). The fundamental laser is initially polarized in vertical direction, and an analyzer is placed before the photon multiplier tube to selectively collect SHG signals with parallel polarization and cross polarization.

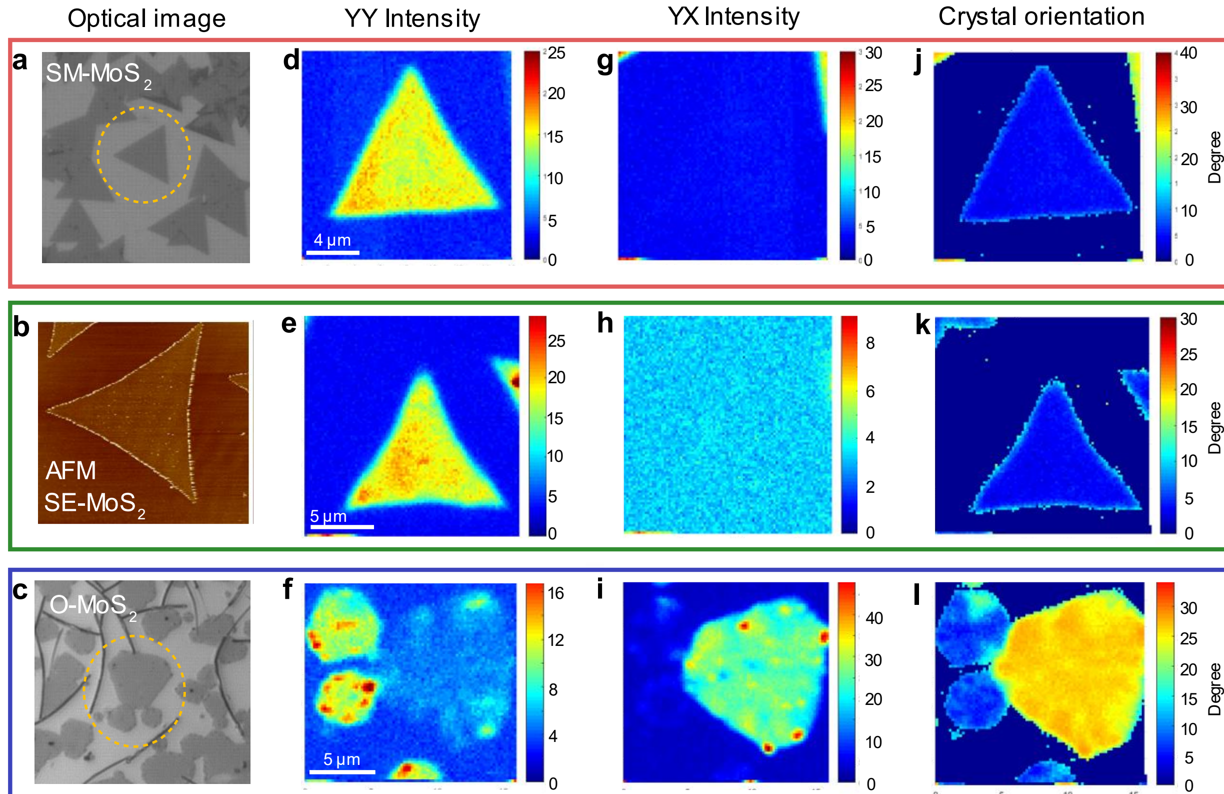

Supplementary Figure 5. Second harmonic generation (SHG) characterization of the three flake types of MoS_2 deposited at different growth conditions. **a, c,** Optical images of a triangular SM-MoS_2 and a convex O-MoS_2 crystal. **b,** Atomic force microscope image of a concave SE-MoS_2 crystal. The corresponding SHG images under (d-f) parallel (*YY*) and **g-i,** cross (*YX*) polarizations. **j-l,** Maps of the crystalline orientation angle θ calculated from (d-f) and (j-l). In (l), the crystalline orientations of the two small flakes are different from the larger flake on the right.

Monolayer MoS_2 grown at different conditions results in various crystal shapes (i.e. concave SE-MoS_2, triangular SM-MoS_2, and convex O-MoS_2). SHG measurements are conducted to confirm whether these three types of MoS_2 flakes are single-crystalline. As shown in Supplementary Fig. 5, the SHG intensity is dependent on the alignment between the polarization of the light (*YY* polarization and *YX* polarization) and the crystal orientation. For example, the SHG intensities are strong under parallel polarization (*YY*), but are close to zero for SE-MoS_2 and SM-MoS_2 crystals, because the polarization of the laser is along the armchair direction of these domains. On the other hand, due to different crystalline orientations, the large domains and the two small domains for the O-MoS_2 sample show the opposite trends for the *YY* and *YX* polarization maps. The non-uniformity of each of the *YY* and *YX* polarization maps in each domain is due to stronger scattering of the particles. From the ratio of these two intensity maps, we can extract the crystal orientations as shown in Supplementary Fig. 5 j, k, l. We can see good uniformity for all three types of samples in terms of the crystal orientations, even though the *YY* or *YX* intensity maps might be non-uniform.

3. Transmission electron microscope (TEM) of monolayer O-MoS_2

The transmission electron microscope (TEM) is performed using FEI Tecni (G2 Spirit TWIN) under 120 kV. The diffraction images are taken with an aperture size of 1 μm in selected-area electron diffraction (SAED). The TEM sample is prepared by direct delamination of the CVD O-MoS_2 from a SiO_2/Si substrate in deionized water, and then transferring the film onto Protochips C-Flat TEM grid (2/4).

4. Raman spectroscopy for doping and strain characterization of monolayer MoS_2

Raman spectroscopy is a powerful non-destructive technique for identifying the number and orientation of layers, and probing material properties of MoS_2 flakes including strain, doping, and defects. Raman characterization of monolayer MoS_2 flakes is carried out by a confocal Raman system of HR800 (Horiba Scientific) with a laser wavelength of 532 nm at the laser power of 2.5 mW and accumulation time of 0.5 sec under air-ambient conditions (1 mW and 1 sec for the

photoluminescence spectra). The emitted Stokes Raman signal is collected by a 0.9 N.A. 100X objective from Carl Zeiss Microscopy GmbH with a 1800 lines/mm grating. The spectrum is calibrated by the Si peak at 520.6 cm^{-1} from an undoped silicon wafer. Monolayer MoS_2 exhibits two Raman characteristic features: out-of-plane vibrational mode of A_{1g} and in-plane vibrational mode E^1_{2g} with a frequency difference of < 21 cm^{-1}.[1] Since the shift rate of A_{1g} and E^1_{2g} are sensitive to strain and doping perturbations, respectively, we can project the orthogonal basis with the vectors of A_{1g} Raman shift and E_{2g} Raman shifts onto the non-orthogonal vectors of strain and carrier concentration. The deconvolution of strain and doping in MoS_2 Raman spectrum are described in the following.[2,3]

MoS_2 exhibits two characteristic features: out-of-plane vibrational mode of A_{1g} at around 405 cm^{-1} and in-plane vibrational mode E_{2g} at around 385 cm^{-1}. Since the shift rates of two vibrational modes are different in strain (***S***) and doping (***P***) perturbations, we can project the orthogonal basis with the vectors of A_{1g} Raman shift (e_A) and E_{2g} Raman shifts (e_E) onto the non-orthogonal vectors of strain (e_ε) and carrier concentration (e_n). The deconvolution of strain and doping in MoS_2 Raman spectrum can be described by

$$\begin{pmatrix} e_\varepsilon \\ e_n \end{pmatrix} = \begin{pmatrix} S_A & S_E \\ P_A & P_E \end{pmatrix} \begin{pmatrix} e_E \\ e_A \end{pmatrix}$$

Where the matrix elements denote the Raman shifts of the A_{1g} and E_{2g} modes as the function of biaxial strain and carrier concentration:

$$S_A = \frac{\Delta\omega_A}{\Delta\varepsilon} = -0.4 \text{ cm}^{-1} / \%$$

$$S_E = \frac{\Delta\omega_E}{\Delta\varepsilon} = -2.1 \text{ cm}^{-1} / \%$$

$$P_A = \frac{\Delta\omega_A}{\Delta n} = -2.22\times10^{-13} \text{cm}^{-1} / \text{cm}^{-2}$$

$$P_E = \frac{\Delta\omega_E}{\Delta n} = -0.33\times10^{-13} \text{cm}^{-1} / \text{cm}^{-2}$$

Therefore, based on the shifts of A_{1g} and E_{2g} modes, the strain and doping concentration for monolayer MoS_2 crystals can be calculated.

As shown in Supplementary Figure 6, the scatter plots for different types of MoS_2 displays distinct characteristics. When compared to the baseline condition (i.e. SM-MoS_2) or the flake grown at a sulfur-excess condition, O-MoS_2 tends to exhibit a negative change in n-type doping (blueshift in A_{1g} peak), that is, the built-in electron density is reduced when oxygen lattice is incorporated with oxygen with a non-uniform distribution of strain.

The variation in growth conditions results in different strain distributions over the MoS_2 crystals. For CVD MoS_2 crystals grown on SiO_2, the samples typically exhibit tensile strain due to the smaller thermal expansion coefficient of SiO_2 than that of MoS_2.[14] The larger thermal expansion coefficient of MoS_2 makes the MoS_2 lattice shrink more than the underlying SiO_2 as it cools down from a high temperature in the growth process, resulting in built-in tensile strain in the as-grown MoS_2. The presence of tensile strain in MoS_2 could not only lead to electronic performance degradation,[86] but also alter the PL characteristics. For example, previous studies have reported a reduction of bandgap with a rate of 45 meV/% uniaxial tensile strain and 100 meV/% biaxial tensile strain for monolayer MoS_2, and a pronounced strain-induced PL quenching due to the direct-to-indirect transition of MoS_2 bandgap.[4,5] As shown in Supplementary Fig. 7b,c, the in-plane vibrational (E^1_{2g}) mode-derived mapping indicates that there exists tensile strain in both SM-MoS_2 and SE-MoS_2 flakes. For the SE-MoS_2 sample, the tensile strain distribution is non-uniform, strongly centralizing on the interior area (~ 0.25 %) and relaxing towards the edges. Correspondingly, the PL mapping of the SE-MoS_2 shows a redshifted PL energy towards the interior (~1.82 eV, Fig. 2e) due to the strain-induced bandgap reduction. The SM-MoS_2 sample exhibits a similar strain characteristic but with a more uniform strain distribution in its interior, and the similar strain-induced redshift of the PL energy from the edge to the interior is also observed (Fig. 2d). The combined effects of electron doping and strain together contribute to the shift in PL energy and the decrease in PL intensity for SM-MoS_2 and SE-MoS_2 crystals shown in Fig. 2a.

On the other hand, there exists strong tensile strain along the edges of the O-MoS_2 crystal, whereas the strain reduces in the interior. The high tensile strain at the edges of O-MoS_2 crystal also leads to a redshift in PL energy around the edges (1.86 eV, Fig. 2c), while the PL energy in the interior shifts to a close-to-A-exciton energy of 1.88 ~ 1.90 eV as the results of its lower electron doping and the relaxed strain. Intriguingly, a 3-fold symmetric distribution of the strain is

observed in the O-MoS_2 crystal. Similar 3-fold symmetric patterns were also observed in high-power-laser-irradiated monolayer CVD WS_2 by Sheng *et al*.[6] It was found that in a hexagonal domain (or truncated triangle) the regions with short (truncated) edges are more favorable to be oxidized. We thus infer that the unique strain profile observed in the O-MoS_2 crystals is likely to originate from the preferential distribution of oxygen dopants during the CVD growth. Supplementary Fig. 7d-f shows the PL intensity mapping of the three types of MoS_2 flakes shown in Fig. 2c-e.

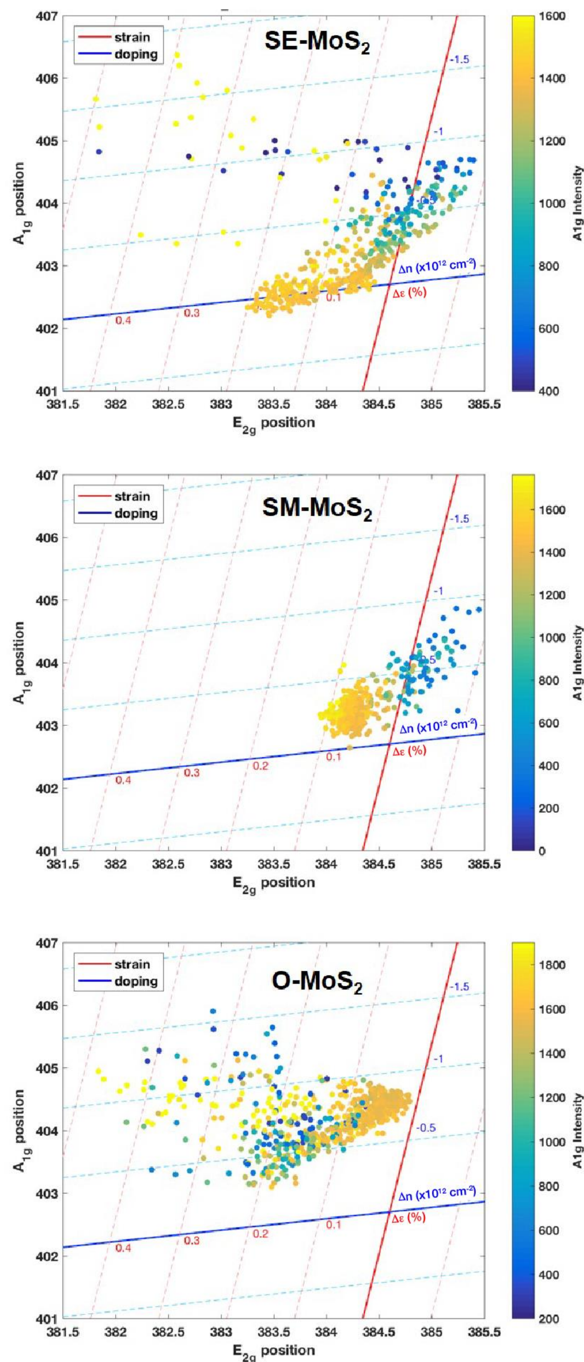

Supplementary Figure 6. Raman-derived changes in strain and carrier density for monolayer MoS_2 flakes grown at different conditions (sulfur excess: SE-MoS_2, sulfur mild: SM-MoS_2, oxygen incorporation: O-MoS_2).

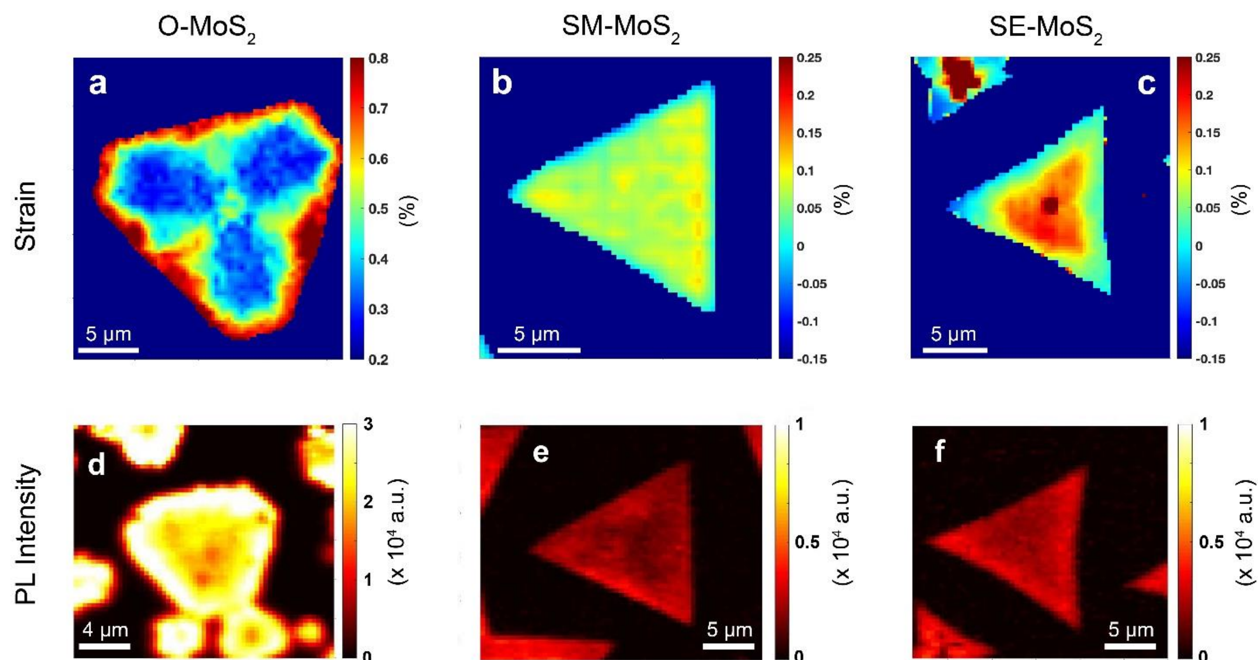

Supplementary Figure 7. a-c, Mapping of strain based on E^1_{2g} shift for the three flake types of MoS_2 crystals grown at different conditions. **d-f,** PL intensity mapping of the three flake types of MoS_2 crystals.

5. X-ray photoelectron spectroscopy (XPS) measurement

The XPS measurement is carried out by using a PHI Versaprobe II XPS instrument with monochromated Al kα source (1486.6 eV) and spot size of 200 μm. 50 W gun power and 15 kV operation voltage are used during spectrum acquisition. Prior to the measurement, the O-MoS_2 sample is carefully rinsed by deionized water and isopropyl alcohol to remove precursor MoO_x cluster attached during the CVD growth. During the measurement, samples are flooded with electron and Ar ion guns to compensate the surface charging.

Our XPS fitting analysis follows several criteria. The peak separation in each doublet peak should be fixed, and the full width at half maximum (FWHM) for the doublet peaks should be the same. Meanwhile, the peak area ratio is assigned based on the degeneracy of the spin state. All of the XPS spectra are calibrated by C1s peak at 284.5 eV. The criteria used for the fitting analysis are listed below: (1) The peaks have specific area ratios based on the degeneracy of spin state (see Supplementary Table 1) j = l + s (j: spin state, l: angular momentum quantum, s: spin angular

momentum) (2) Splitting doublet S $2p_{3/2} - 2p_{1/2}$ doublet separation is ~1.2 eV; Mo $3p_{5/2} - 3p_{3/2}$ doublet separation is ~3.13 eV (3) Atomic subshell asymmetry parameter is applied (4) Background is fitted using Shirley method (5) 20% Lorentzian-Gaussian (20LG) is used for the fitting function.

Supplementary Table 1. The peak area ratios of spin-orbit splitting at different subshells

Subshell	j values	Area Ratio
s	1/2	n/a
p	1/2 3/2	1:2
d	3/2 5/2	2:3
f	5/2 7/2	3:4

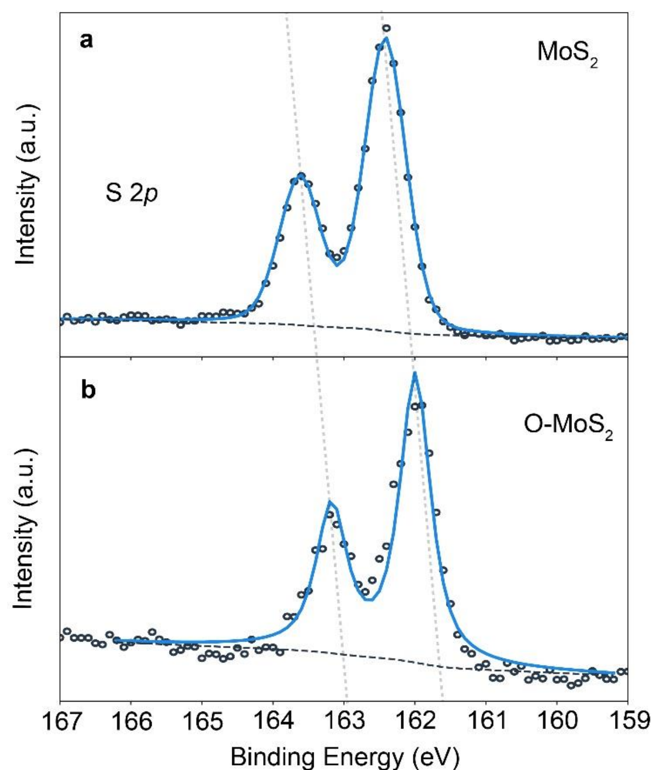

Supplementary Figure 8. XPS spectra of S 2p core level for a typical CVD MoS_2 film grown under a sulfur-mild condition and an O-MoS_2 film. The XPS spectrum for the O-MoS_2 sample shifts to lower binding energies, suggesting a downward shift in Fermi level.

6. Electrostatic force microscope (EFM) characterization of monolayer MoS_2

Electrostatic force microscopy (EFM) is a technique that is sensitive to the electric force between the sample and the tip, and therefore the electrical properties of the sample. The most common implementation is a two-pass technique, where the topography is obtained in the first pass before lifting the tip above the surface, where long range forces (i.e. electromagnetic) dominate, maintaining a constant height above the surface while recording the phase shift ($\Delta\theta_{\text{electrical}}$) of the oscillating tip. This phase shift is measured relative to the driving oscillation to the piezo that mechanically excites the tip.

Any force that the tip experiences will alter the resonance frequency, and this change in resonance frequency $\Delta\omega_{res}$ depends on the derivative of the force.

$$\Delta\omega_{res} = \frac{\omega_{res}}{2k} \cdot \frac{\partial F}{\partial z} \quad (1)$$

This equation is valid for small $\partial F/\partial z$, where ω_{res} is the resonance frequency without that force, k is the tip spring constant, z is the tip-sample distance, and for the electrical force that determines the EFM contrast is given by

$$\frac{\partial F_{electrical}}{\partial z} = \frac{1}{2}\frac{\partial^2 C}{\partial z^2}\left[\Delta V\right]^2 \quad (2)$$

where C is the tip-sample capacitance, and ΔV can have contributions from applied voltages to the tip and the sample, work function differences, and trapped charges. To convert $\Delta\omega_{res}$ into a phase shift, we need to know the quality factor of the cantilever.

For EFM, the phase shift is given by

$$\Delta\theta_{electrical} = -\frac{Q}{2k}\frac{\partial^2 C}{\partial z^2}\left[\Delta V\right]^2 \quad (3)$$

where Q is the tip quality factor. Note that the phase shift is dependent on the second derivative of the capacitance with respect to z,[7] which is why EFM generally provides higher lateral resolution than KPFM (which depends on the first derivative).[8] EFM measurements are less sensitive to the undesirable coupling between the cantilever and the sample, beyond the portion of the sample directly beneath the tip. This is especially important for samples where the region of interest is small compared to the length of the cantilever.

Assuming that there are no trapped charges and that the sample is grounded, the phase shift can be written as

$$\Delta\theta_{electrical} = -\frac{Q}{2k}\frac{\partial^2 C}{\partial z^2}\left[V_{tip} - V_{CPD}\right]^2 \quad (4)$$

where V_{tip} is the DC voltage applied to the tip, and V_{CPD} is the contact potential difference between the sample and the tip given by

$$V_{CPD} = \frac{\varphi_{sample} - \varphi_{tip}}{e} \quad (5)$$

Here, e is the magnitude of charge on the electron and φ_{sample} and φ_{tip} are the sample and tip work functions respectively.

The phase shift is parabolic with the tip voltage V_{tip} as seen in Supplementary Fig 8b, with the minimum phase shift occurring when $V_{\text{tip}} = V_{\text{CPD}}$. If the tip and sample were the same material, we would expect the minimum to occur for $V_{\text{tip}} = 0$. Since they are different materials in this work, the minimum occurs when the voltage of the tip corresponds to the difference in work function.

To reliably extract quantitative information about work function from EFM scans, we perform multiple scans at different tip voltages, always including a known reference material (Au) in the same scan as the MoS_2. Supplementary Fig. 9a shows scans of the phase shift with $V_{\text{tip}} = -5$ V and 3 V, revealing a clear difference in contrast at these two V_{tip}. We plot the phase shift at each tip voltage for MoS_2 and Au, which we then fit to a parabola to extract the minimum

(Supplementary Fig. 9b). The difference in the minima is proportional to the difference in work function between Au and MoS_2.

To extract the phase shift ($\Delta\theta_{electrical}$) for each material from a scan at a fixed V_{tip}, we exclude all but a representative portion of the image. This removes the contribution from the interface between materials, as well as the beginning of the scan. We generate a histogram of the phase values, which contains either only MoS_2 or only Au. By fitting the histogram to a Gaussian, we obtain values for the mean and standard deviation for $\Delta\theta_{electrical}$. After completing this analysis for each V_{tip} image, the resulting parabolic fits (solid curves in the inset in Supplementary Fig. 9b) reveal that V_{CPD} is more positive for O-MoS_2 than for Au for the data shown. The dashed lines in the inset of Supplementary Fig. 8b mark the tip voltages associated with minimum phase shifts for Au (in gold) and O-MoS_2 (in purple). By using the gold as a reference, we know that

$$\varphi_{MoS_2} = \varphi_{Au} + e\Delta V_{CPD} \tag{6}$$

Taking the work function of a grounded Au electrode to be 5.2 eV, we find the average work function of the O-MoS_2 to be 5.45 ± 0.05 eV and of the SM-MoS_2 to be 5.19 ± 0.05 eV, as shown in Fig. 4c. Error bars are the standard deviation around the average work function from multiple sets of scans taken at different flake locations.

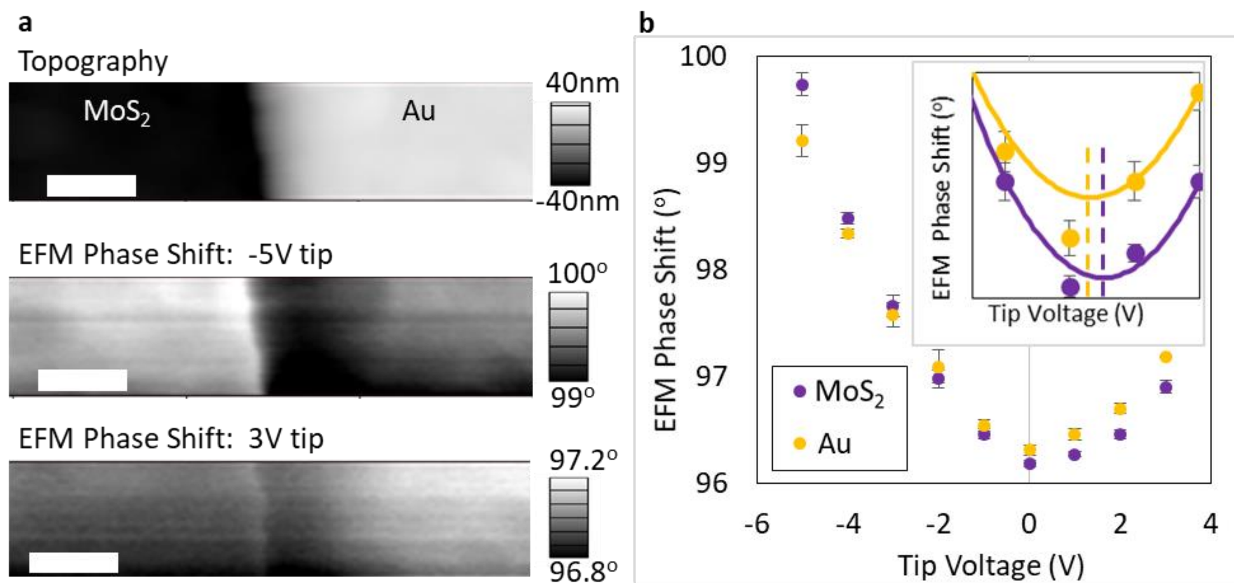

Supplementary Figure 9. Variation in EFM phase shift as a function of tip voltage. **a,** Topography (top) scan over the interface between O-MoS_2 and Au and EFM phase shift scans taken over the same region with a -5 V (middle) and 3 V (bottom) tip voltage. Scale bar is 100 nm for all three images. **b,** EFM phase shift relative to the original piezo excitation as a function of tip voltage for O-MoS_2 (purple) and Au (gold). Error bars are the standard deviation in the EFM phase shift $\Delta\theta_{electrical}$ for each V_{tip} scan. Inset: magnified plot with tip voltages from -1.5 V to 2 V, at voltages near the minima in phase shift for O-MoS_2 and Au which are marked with dashed lines. Solid lines are parabolic fits to the data.

The work functions for doped MoS_2 flakes are measured with an Asylum Research MFP-3D atomic force microscope while flowing dry nitrogen over the sample. Adama Innovations super sharp conductive single crystal diamond tips (AD-40-SS) with a resonant frequency of 180 kHz and a spring constant of 40 N/m are used to take the EFM measurements using an amplitude modulated two pass technique. The Au top electrodes and back gate of the FET are grounded for all EFM scans to allow for comparison between the MoS_2 work functions extracted from different sets of EFM scans.

7. First-principles calculation

The first-principles calculations of the electronic structure are carried out based on the spin-polarized density functional theory (DFT) employing periodic boundary conditions as implemented in the Vienna ab initio simulation package (VASP). The projector augmented wave (PAW) pseudopotentials and the generalized gradient approximation (GGA) functional of Perdew, Burke, and Ernzerhof (PBE) are used with spin-orbit coupling included. An orthorhombic supercell with $16.5 \times 15.85 \times 20$ Å is constructed to guarantee the isolation of single point defects, such as sulfur vacancy (Vs) and oxygen-replaced sulfur vacancy (Os). Relaxation is first performed with $5 \times 5 \times 3$ Gamma centered mesh until the Hellman-Feynman force has been reduced to lower than 0.05 eV/Å and a finer mesh of $11 \times 11 \times 3$ is used to calculate density of states (DOS) and band structure. Dipole corrections are included in the calculation of work function.

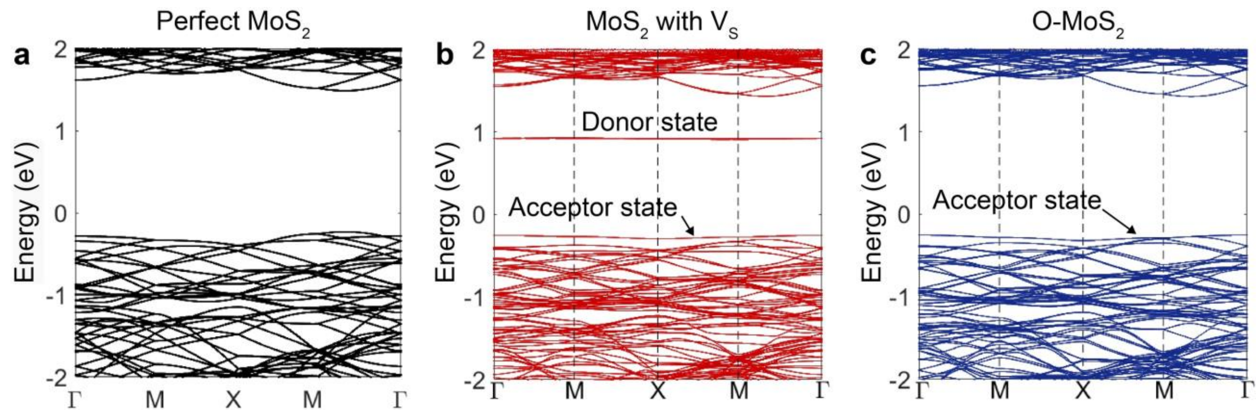

Supplementary Figure 10. **a,** Electronic band structure of perfect monolayer MoS_2. **b,** Electronic band structure of defective monolayer MoS_2 with sulfur vacancies. **c,** Electronic band structure of monolayer O-MoS_2 possessing single oxygen atoms bound to the sulfur vacancy sites.

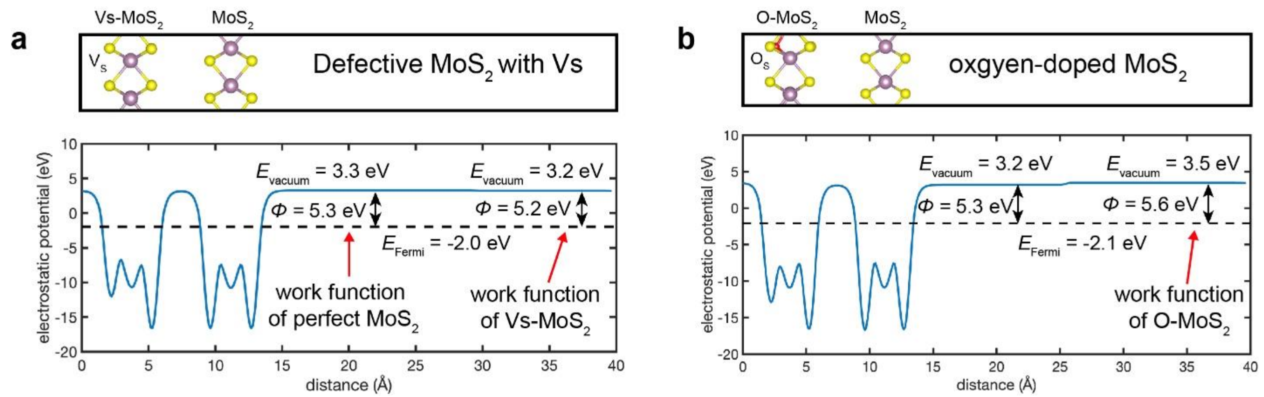

Supplementary Figure 11. a, b, DFT calculations of work functions for defective MoS_2 (with sulfur vacancies) **(a)** and oxygen-doped MoS_2 (sulfur vacancies passivated by oxygen atoms, as shown by the red atom on the top left of the upper panel) **(b)**, illustrating the effects of sulfur vacancy and oxygen dopant on MoS_2 work function. The pristine MoS_2 has a work function of 5.3 eV (from ~15 to ~25 Å of each electrostatic potential plot). The presence of sulfur vacancies lifts the Fermi level, decreasing the work function. This suggests that sulfur vacancies act as donors in MoS_2. On the other hand, the presence of oxygen dopants bound to the sulfur vacancy sites in MoS_2 increases the work function. These results well agree with the EFM characterization.

8. Monolayer MoS_2 FET fabrication and characterization

The CVD-grown monolayer MoS_2 is transferred onto a 300 nm SiO_2/p^{++}-Si substrate serving as the dielectric and gate electrode by a wet transfer process. First, poly-methyl methacrylate (950 PMMA A6) is spin-coated (4000 rpm for 1 min) onto the as-grown monolayer MoS_2 samples. Next, the PMMA/MoS_2/SiO_2/Si stack is placed in a diluted hydrofluoric acid (HF) solution. After the SiO_2 layer is etched away, the PMMA/MoS_2 stack is separated from the substrate and remains floating on the solution. The PMMA/MoS_2 film is then placed in deionized water to remove the HF residue. This rinsing step is repeated three times. After that, the PMMA/MoS_2 film is transferred onto the 300 nm SiO_2 substrate, and is then baked at 70 °C for 20 min and 130 °C for another 20 min. This baking step can remove moisture and enhance the adhesion between MoS_2 and the substrate. Finally, the PMMA/MoS_2/substrate stack is immersed in acetone for 6 h to remove the PMMA layer.

After the MoS_2 transfer process, electron-beam lithography is used to define the source and drain contacts and MoS_2 channel, followed by electron-beam evaporation of 20-nm Ni/30-nm Au as the electrical contacts at ~10^{-6} torr. The heavily p-doped silicon wafer serves as the back gate and the 300-nm-thick SiO_2 acts as the gate dielectric. After liftoff using acetone, no further treatment is performed on the devices. The electrical measurements of transistors are carried out in a vacuum environment (10^{-6} torr) in a Lakeshore probe station using an Agilent semiconductor parameter analyzer.

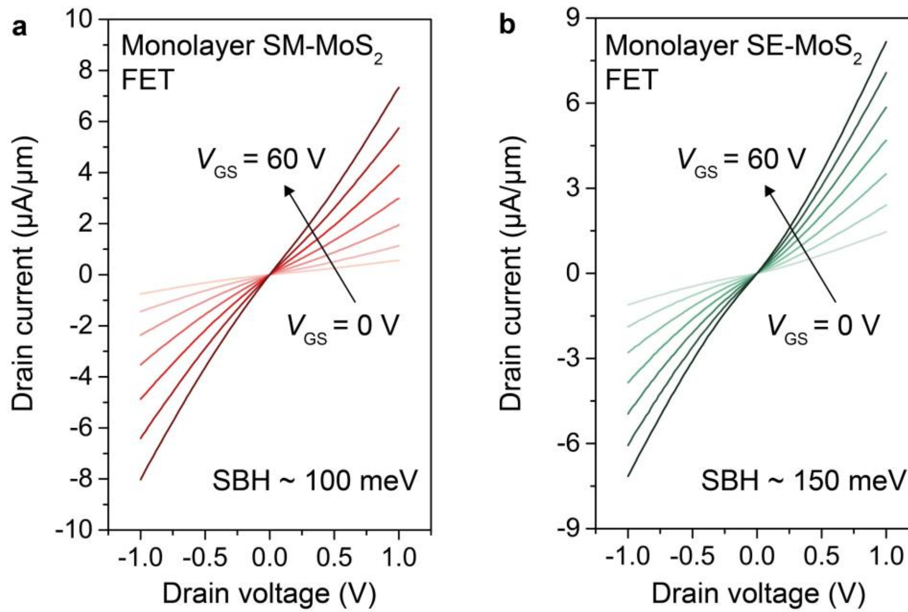

Supplementary Figure 12. **a, b,** Room-temperature output characteristics of the transistors based on monolayer MoS_2 grown at sulfur-mild (SM-MoS_2) and sulfur-excess (SE-MoS_2) conditions, respectively, with Ni contacts. V_{GS} changes from 0 V to 60 V in steps of 10 V.

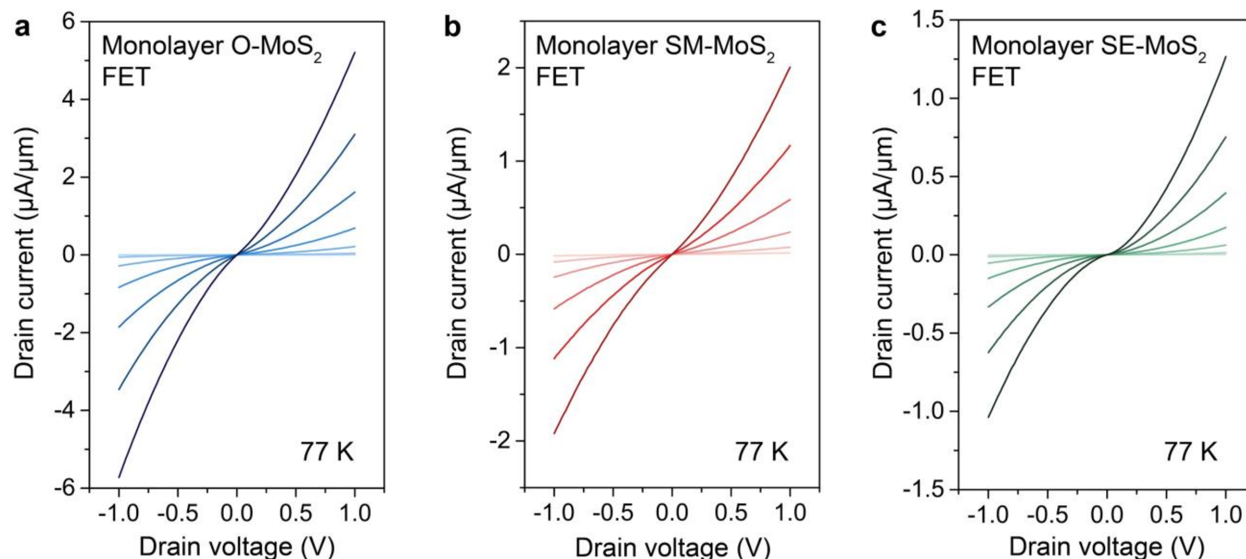

Supplementary Figure 13. a-c, Output characteristics at 77 K for the same transistors in Fig. 4d and Supplementary Fig. 11. I_{DS}-V_{DS} curves of monolayer O-MoS_2, SM-MoS_2, and SE-MoS_2 transistors with Ni contacts for various V_{GS} ranging from 0 V to 60 V in steps of 10 V. The nonlinear characteristics observed at low temperatures from all these types of transistors indicate the presence of Schottky barriers at their contact interfaces.

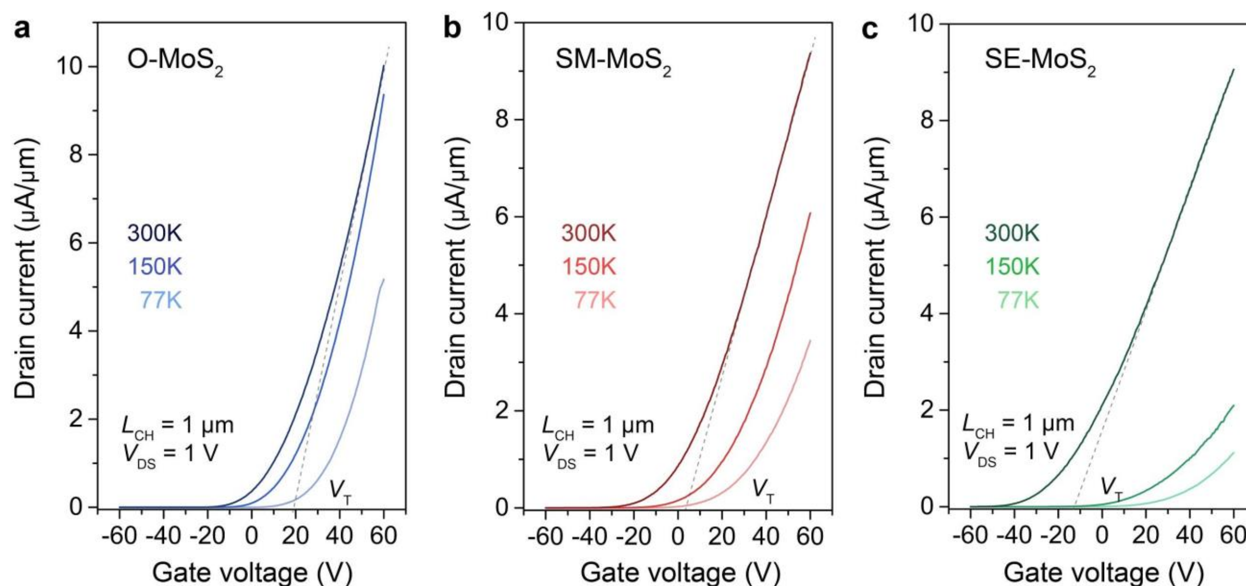

Supplementary Figure 14. a-c, Transfer characteristics of FETs with O-MoS_2, SM-MoS_2, and SE-MoS_2 flakes at various temperatures (V_{DS} = 1 V). The drain current decreases with decreasing

temperature due to the suppressed thermionic emission current across the contact barrier. Note that the lower sensitivity of I_{DS} to the decrease in temperature for the O-MoS_2 FET suggests a lower contact barrier compared to the devices with MoS_2 grown without oxygen. The dashed line shows the V_T extracted at the maximum transconductance (g_m) of the transfer curve.

9. Threshold voltage and mobility extraction

The threshold voltage (V_T) of a transistor is extracted at the interception of the linear fitting of the transfer characteristic (I_{DS}-V_{GS}) curve with maximum transconductance (g_m= dI_{DS}/dV_{GS}) (Supplementary Fig. 14), where I_{DS} and V_{GS} are the drain current and the gate voltage, respectively. This is called the extrapolation in the linear region (ELR) method for semiconductor device analysis. The field-effect mobility can be calculated by $\mu = g_m[L_{CH}/(WC_{ox}V_{DS})]$, where C_{ox} is the capacitance per unit area of the gate dielectric (~1.15×10^{-8} F/cm^2 for the 300-nm-thick SiO_2 dielectrics used in this study), L_{CH} is the channel length, and W is the channel width.

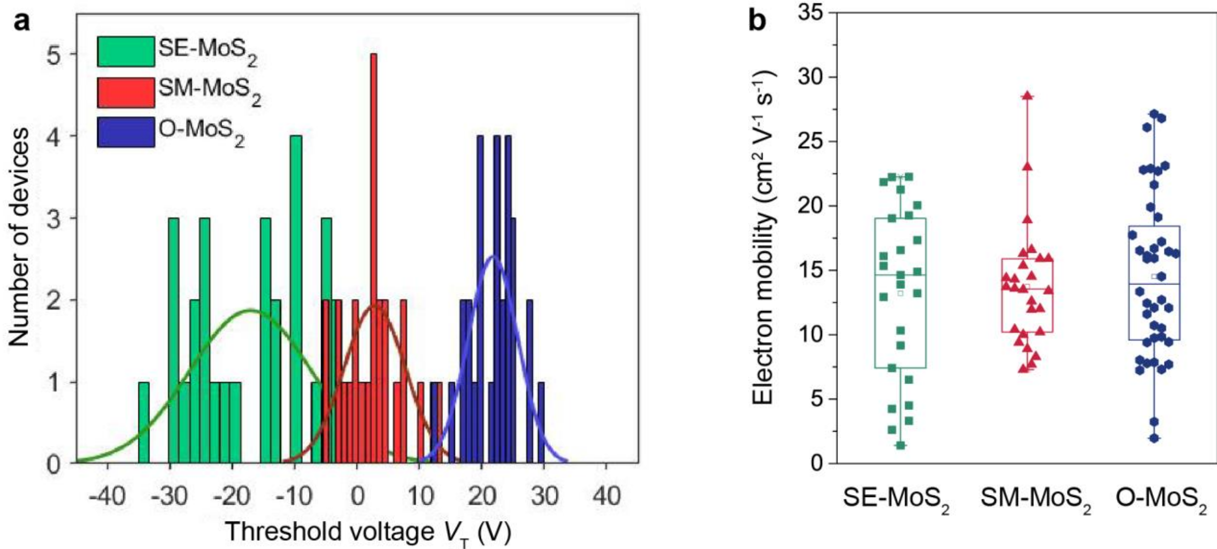

Supplementary Figure 15. a,b, Statistical distribution of V_T and field-effect mobility (μ) for the three flake types of monolayer MoS_2 transistors. The average V_T for SE-MoS_2, SM-MoS_2, and O-MoS_2 transistors are -17 ± 9.7, 2.8 ± 4.9, and 21 ± 4.6 V, respectively. The average μ for SE-MoS_2, SM-MoS_2, and O-MoS_2 transistors are 13.2, 13.7, and 14.5 cm^2 V^{-1} s^{-1}, respectively.

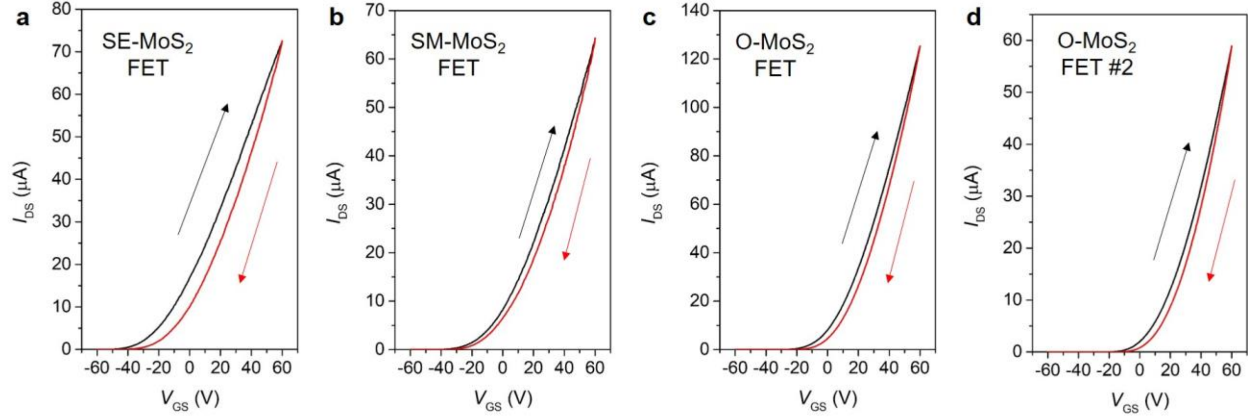

Supplementary Figure 16. a-d, Transfer curves at fixed drain-source bias (V_{DS} = 1 V) with different sweeping direction of the gate voltage for the three flake types of MoS_2 FETs. The reasonably small hysteresis behavior allows reliable V_T extraction. Both sweeping directions yield the same trend of V_T shift as shown in Supplementary Fig. 15.

10. Extraction of Schottky barrier height (SBH) through thermionic emission model

A 2D Schottky FET can be regarded as two Schottky diodes connected back-to-back. Most of the applied drain-to-source voltage (V_{DS}) drops at the reverse-biased contact. Therefore, for a n-channel FET the transistor behavior is dominated by the source side. The drain current (I_{DS}, in units of μA/μm) thermally injected from the metal contact into the 2D channel through a reverse-biased Schottky barrier can be expressed as:

$$I_{DS} = A^*_{2D}T^{1.5}\exp[-(\Phi_B)/(k_BT)][1-\exp((-V_{DS})/(k_BT))] \quad (7)$$

where A^*_{2D} is the Richardson constant for a 2D system, T is the temperature, k_B is Boltzmann's constant, q is the elementary charge, and Φ_B is the effective contact barrier height at a given gate-source voltage (V_{GS}). If $V_{DS} >> k_BT$, equation (7) can be simplified to

$$I_{DS} = A^*_{2D}T^{1.5}\exp[-(\Phi_B)/(k_BT)] \quad (8)$$

In this way, the effective energy barrier at a given V_{GS} can be extracted by fitting the slope in the Arrhenius plots, as shown in Supplementary Fig. 17a-c, using the following equation:

$$\ln(I_{DS}/T^{1.5}) = -\Phi_B/k_BT + c \quad (9)$$

where c is a constant. SBH is then extracted at the flat-band condition ($V_{GS} = V_{FB}$),[9] as shown in Supplementary Fig. 17d-f.

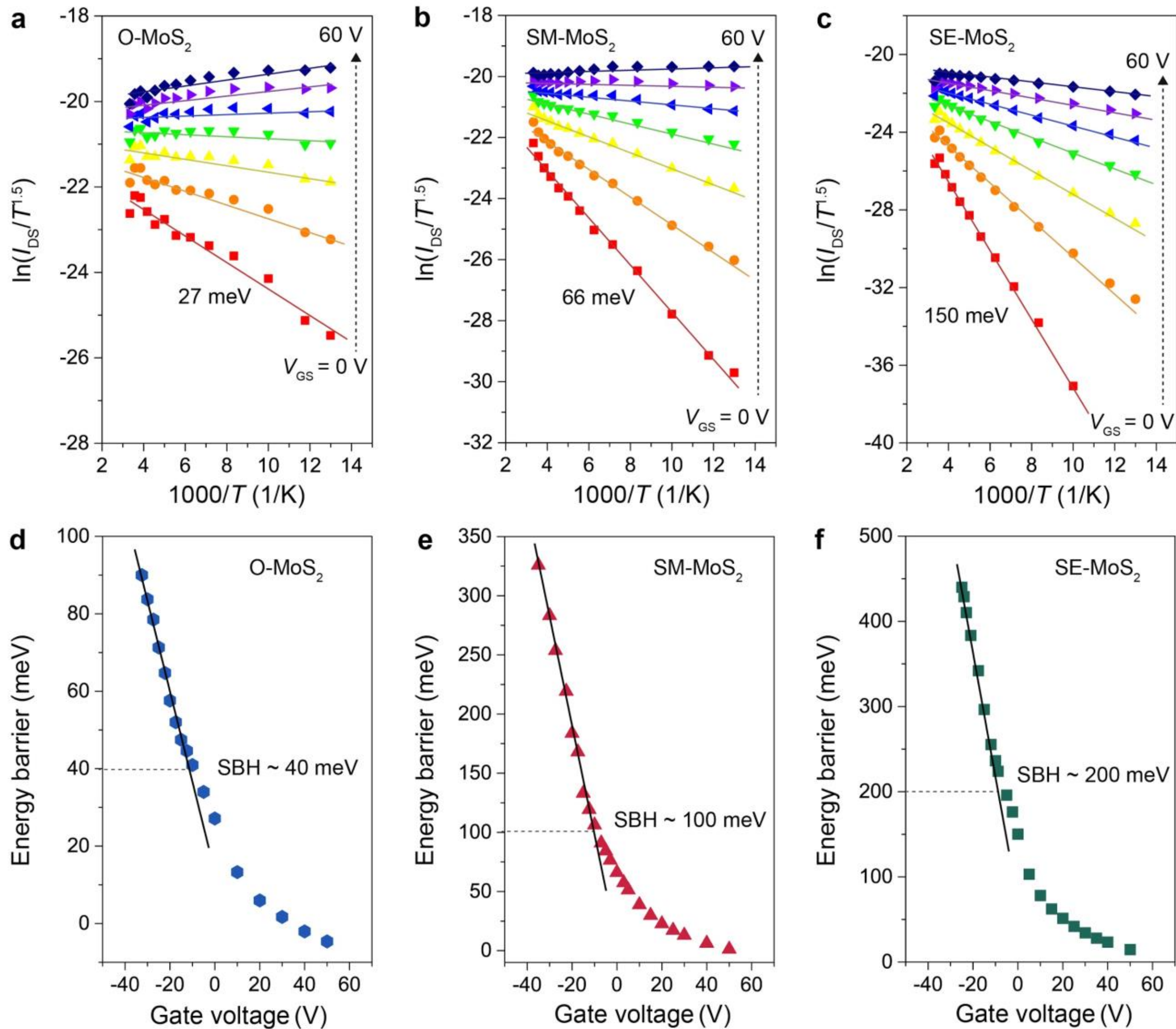

Supplementary Figure 17. a-c, Arrhenius plots and Schottky barrier extraction of Ni-contacted

monolayer MoS_2 FETs with different flake types deposited at different conditions (i.e., with oxygen and sulfur-mild and sulfur-excess environments without oxygen). Colorful solid lines in (a), (b), and (c) are linear fits to the data showing thermally activated behavior. **d-f,** The effective contact barriers at various gate biases for monolayer O-MoS_2, SM-MoS_2, and SE-MoS_2 transistors. Schottky barrier heights (SBH) are extracted at the flat-band condition.

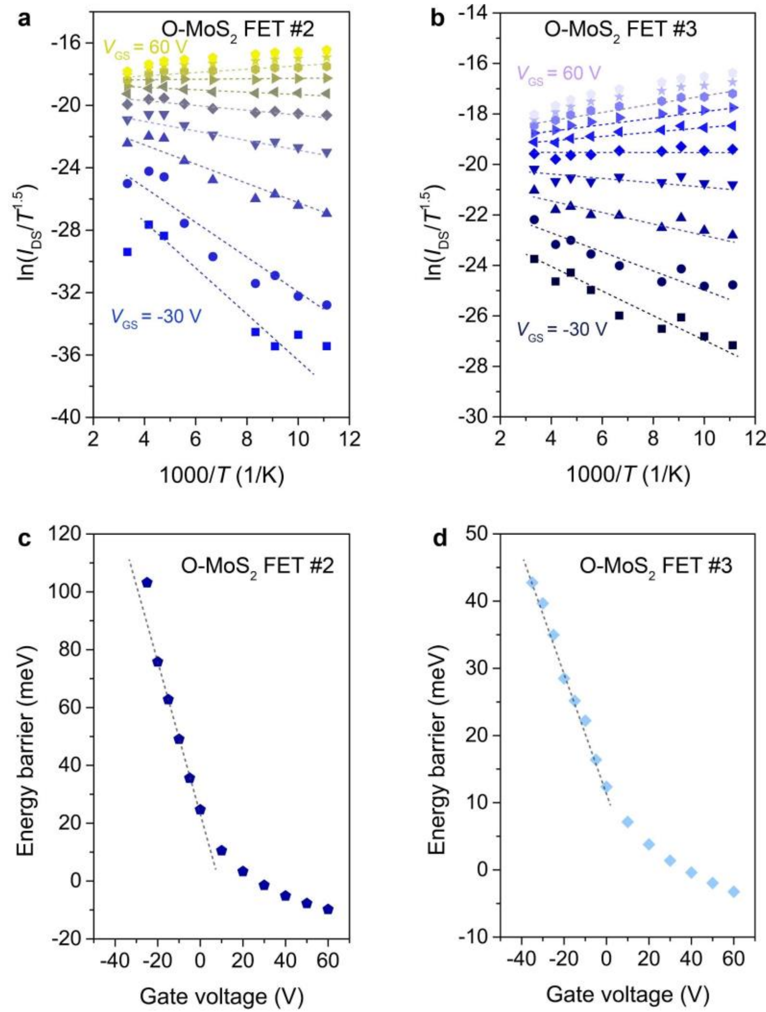

Supplementary Figure 18. a,b, Arrhenius plots of two additional monolayer O-MoS_2 FETs with Ni contacts. **c,d,** Extraction of Schottky barrier heights for the same FETs in (a) and (b), showing the same feature of a low contact barrier in the range of 10 − 40 meV.

11. Extraction of contact resistance and mobility by transfer length method (TLM)

In a 2-terminal semiconductor device, the total device resistance (R_{TOT}, in units of kΩ μm) normalized by channel width (W) can be expressed as $R_{TOT} = 2R_C + R_{CH} = 2R_C + R_{SH}L_{CH}$, where R_C is the contact resistance, R_{CH} is the channel resistance, R_{SH} is the sheet resistance of the channel (in units of kΩ/□) and L_{CH} is the channel length. The total device resistance varies linearly with the L_{CH} if the R_C (in units of kΩ μm) and R_{SH} are spatially homogeneous in the device. Therefore, by measuring the total resistances of the devices with various L_{CH}, the R_{TOT} can be plotted as a function of L_{CH}. In the limit of a device with $L_{CH} = 0$, the residual resistance corresponds to the total contact resistance ($2R_C$) of the device.

Accordingly, we extract the R_C of the MoS_2 transistors for a given carrier density (n_{2D}) by plotting the R_{TOT} versus L_{CH} as shown in Supplementary Fig. 19b. The vertical intercept at $L_{CH} = 0$ of a linear fit yields the $2R_C$ for the two-terminal MoS_2 devices. Also, the R_{SH} of the MoS_2 channel for a certain n_{2D} can be calculated from the slope of the linear fit. The effective mobility is then calculated by $\mu_{eff} = 1/(qn_{2D}R_{SH})$ (Supplementary Fig. 20). The n_{2D} induced by electrostatic gating is estimated by assuming a simple linear charge dependence on the gate voltage overdrive

$$n_{2D} = C_{ox} (V_{GS} - V_T)/q \qquad (10)$$

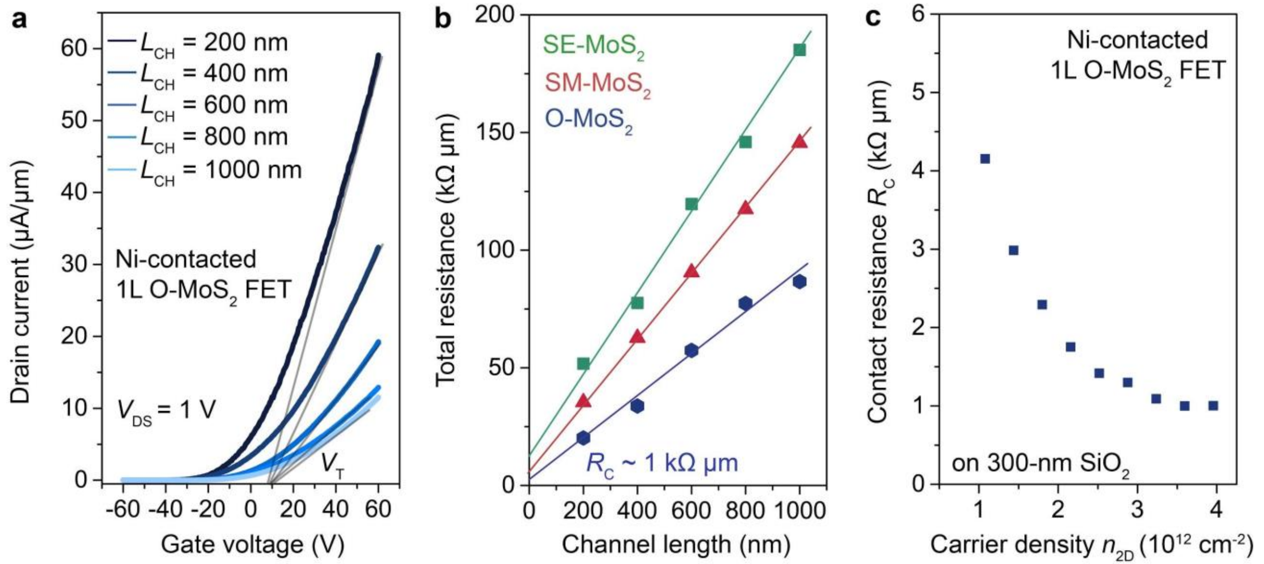

Supplementary Figure 19. a, Transfer curves of Ni-contacted monolayer O-MoS_2 FETs with various channel lengths (L_{CH}) ranging from 200 nm to 1000 nm. The gray lines indicate the linearly extrapolated threshold voltage (V_T). **b,** Contact resistance (R_C) extracted from TLM for the three different types of monolayer MoS_2 transistors with Ni contacts. The R_C are extracted at a carrier concentration of 4×10^{12} cm^{-2} at room temperature. **c,** R_C extracted from TLM as a function of carrier density (n_{2D}) for Ni contact to monolayer O-MoS_2, reaching a lowest R_C of ~ 1 kΩ μm. Overall, the R_C decreases from 4.1 kΩ μm at $n_{2D} = 1 \times 10^{12}$ cm^{-2} to 1 kΩ μm at $n_{2D} = 4 \times 10^{12}$ cm^{-2}. This dependence of R_C on n_{2D} can be attributed to the modulations of width and height of the effective barriers at the interface due to the application of gate voltage.[9]

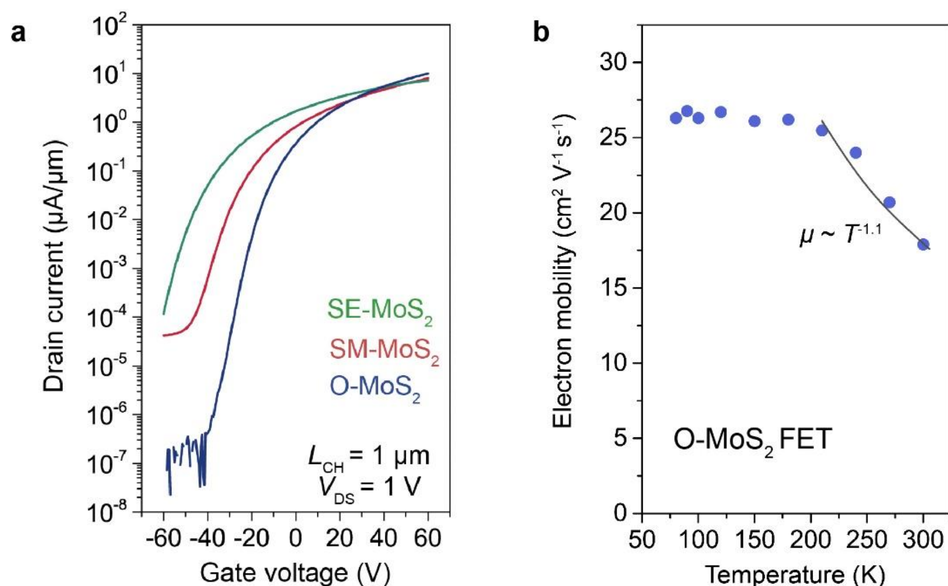

Supplementary Figure 20. a, Transfer characteristics of transistors made with three types of MoS_2, in semilogarithmic scale. **b,** Intrinsic electron mobility μ_{eff} extracted from TLM as a function of temperature (T) for monolayer O-MoS_2 with Ni contacts. The $T^{-1.1}$ dependence suggests the mobility in the device is dominated by phonon scattering in the temperature range of 200 - 300 K, while the dominant scattering becomes impurity-limited at lower temperatures.

12. Optical characterization of defect states in monolayer MoS_2

Temperature dependent photoluminescence (PL) measurements are carried out on a micro-Raman spectrometer (Horiba-JY T64000). The back-scattering signal is collected through a 50× long-working-distance objective and dispersed with a 150 g/mm grating. A cryostat (Cryo Industry of America, USA) is used to provide a vacuum environment and a continuous temperature from 77 to 300 K by liquid nitrogen flow. A 514-nm laser line from a Kr+/Ar+ ion laser (Coherent Innova 70C Spectrum) is used to excite the sample.

Supplementary Fig. 21 summarizes the statistics of the PL spectra of MoS_2 synthesized with the three different conditions. Supplementary Fig. 22 shows typical temperature-dependent PL of the three types of MoS_2 samples. The trends of both the free exciton peak energies (Supplementary Fig. 22e-h) and the relative populations of the bound excitons (Supplementary Fig.

22f) agree well with previous reports. Supplementary Fig. 23 shows the incident laser power dependence of the three types of MoS_2 samples at 78 K. The free exciton peaks undergo a linear relation with the power, whereas the bound exciton peaks increases sublinearly with the power. Supplementary Fig. 24 is additional data of gate voltage dependence of PL for the three types of MoS_2.

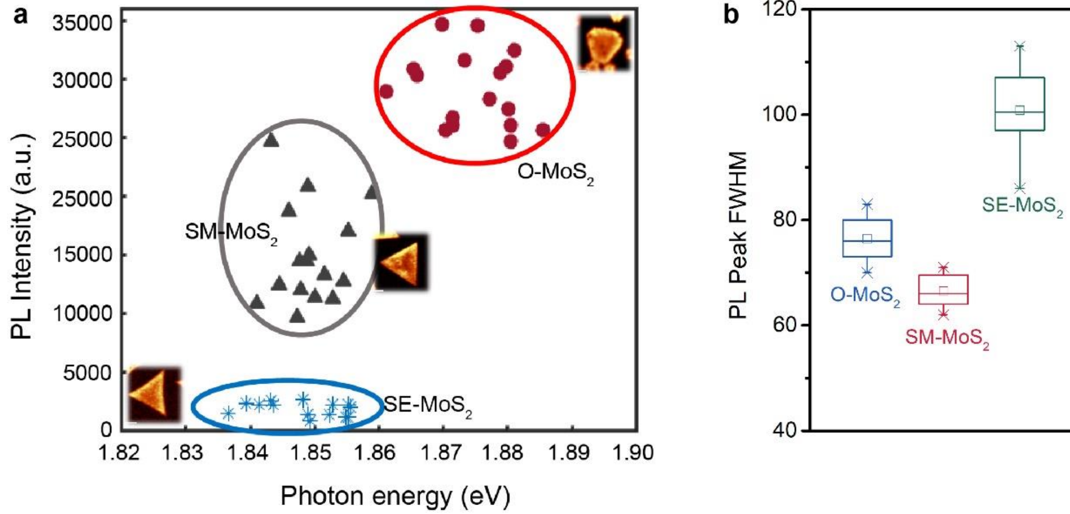

Supplementary Figure 21. a, Statistical illustration of PL intensity vs energy of the three types of monolayer MoS_2. **b,** Full width at half maximum (FWHM) of the PL peaks of the three flake types.

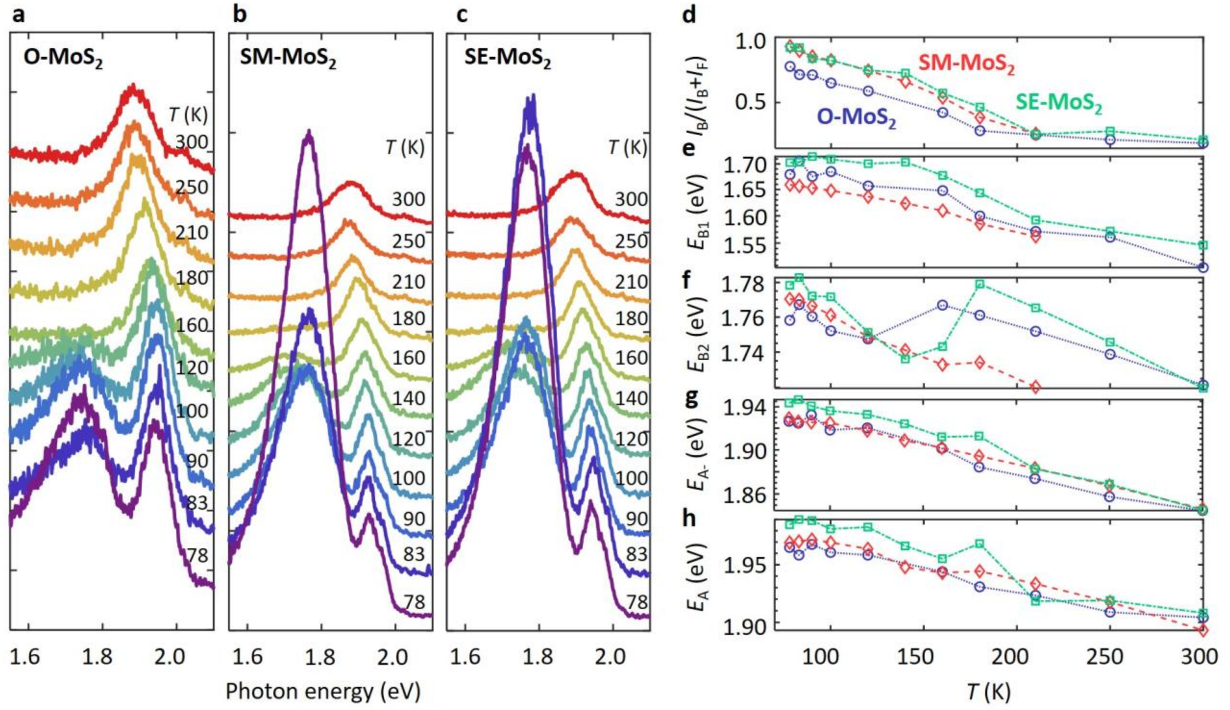

Supplementary Figure 22. Temperature dependent photoluminescence (PL). **a-c,** PL spectra of monolayer O-MoS_2, SM-MoS_2, and SE-MoS_2 with temperature ranging from 78 K to 300 K. **d-h,** Relative bound exciton populations and peak positions of the four exciton peaks as a function of temperature. The parameters for monolayer O-MoS_2, SM-MoS_2, and SE-MoS_2 are plotted as blue circles, red diamonds, and green squares, respectively.

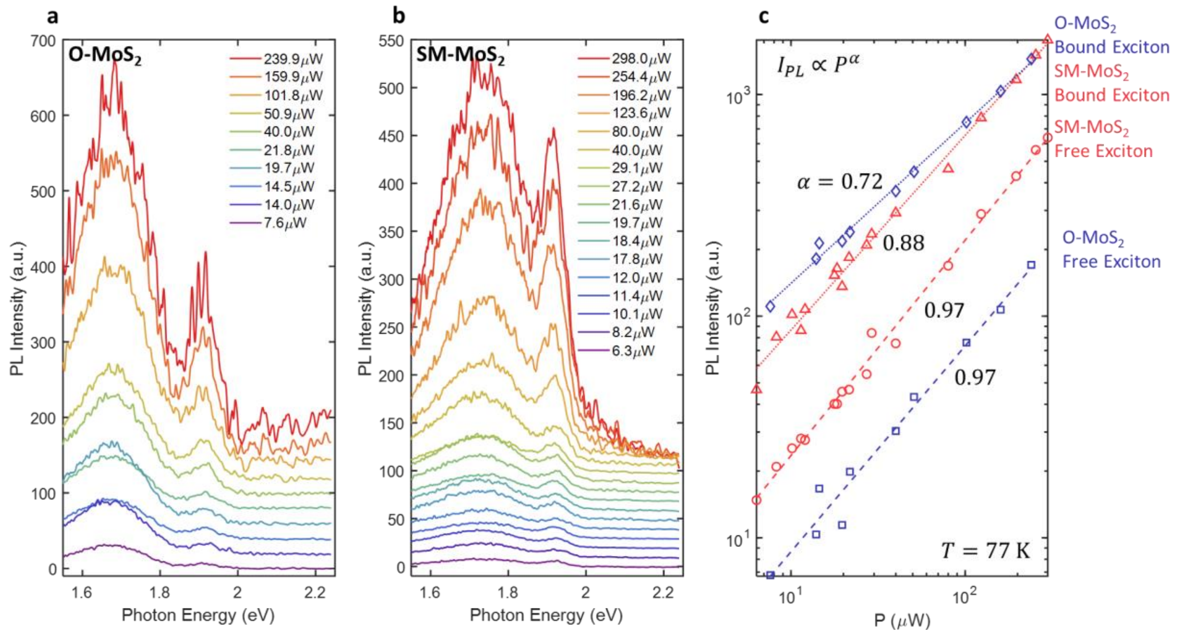

Supplementary Figure 23. Power dependent photoluminescence (PL). **a,b,** PL spectra of monolayer O-MoS_2 and SM-MoS_2 with different laser excitation power. The spectra are normalized with the accumulation time. **c,** Accumulated PL intensities for free excitons (1.85-2 eV, dashed lines) and bound excitons (1.55-1.85 eV, solid lines). The PL intensities for monolayer O-MoS_2 and SM-MoS_2 are plotted in blue and red, respectively.

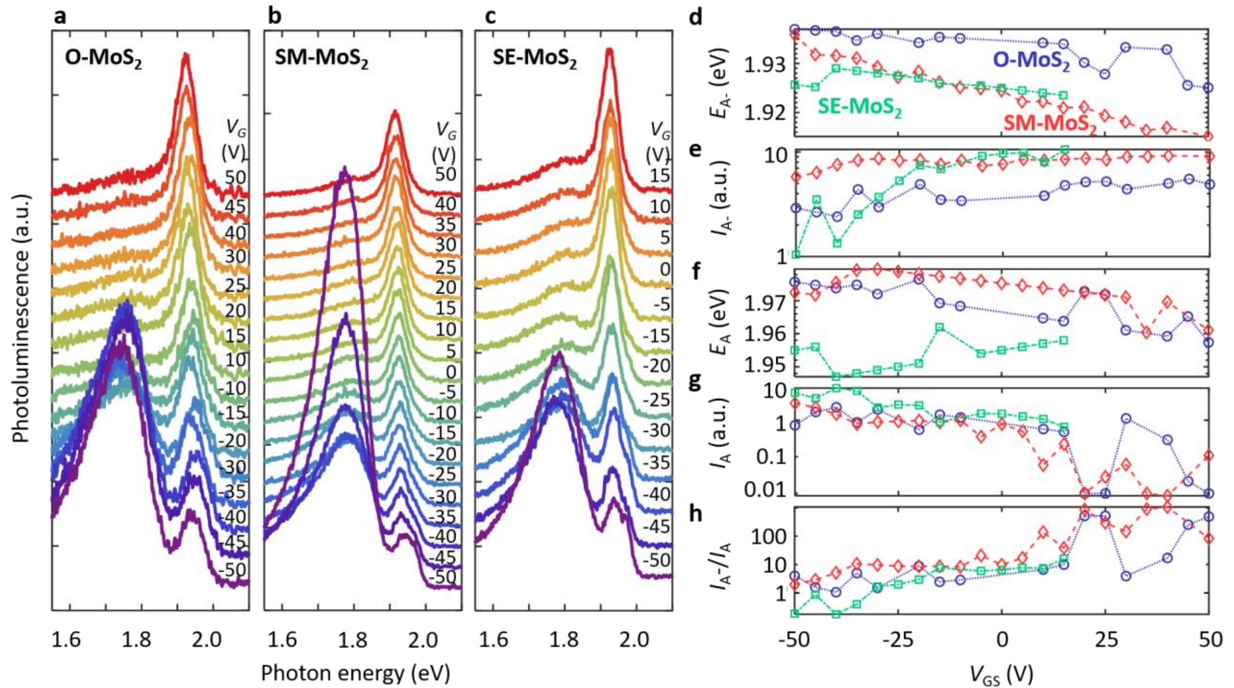

Supplementary Figure 24. Additional data for gate dependent photoluminescence (PL) at 78 K. **a-c,** PL spectra of monolayer O-MoS_2, SM-MoS_2, and SE-MoS_2 with different gate voltages. **d-g,** Peak positions and the accumulated intensities of the free exciton states (X_A^- and X_A) as a function of V_{GS}. The parameters for monolayer O-MoS_2, SM-MoS_2, and SE-MoS_2 are plotted as blue circles, red diamonds, and green squares, respectively. **h,** The trion-to-exciton PL intensity ratio (I_{A^-}/I_A) as a function of V_{GS}.

13. Electrical and optical properties of O-MoS_2 measured in air and in vacuum

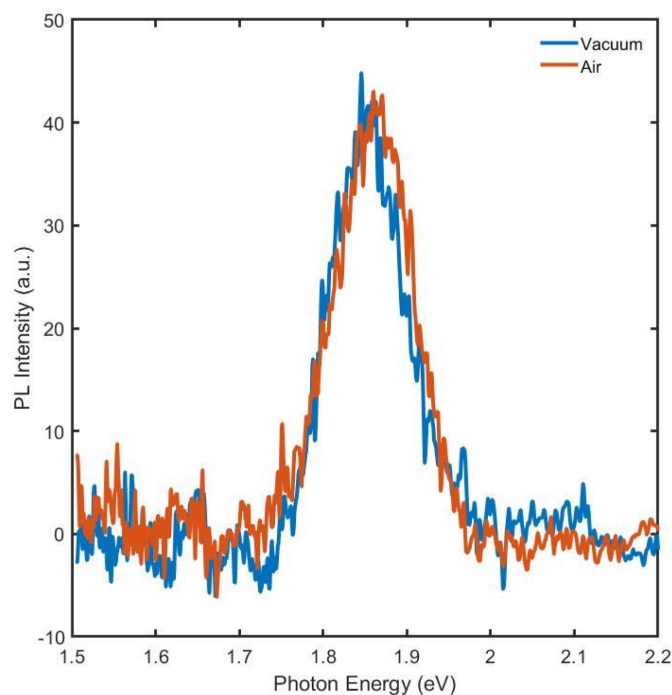

Supplementary Figure 25. Typical PL spectra of O-MoS_2 measured in air and in vacuum. These two spectra were taken at the same position of the O-MoS_2 sample.

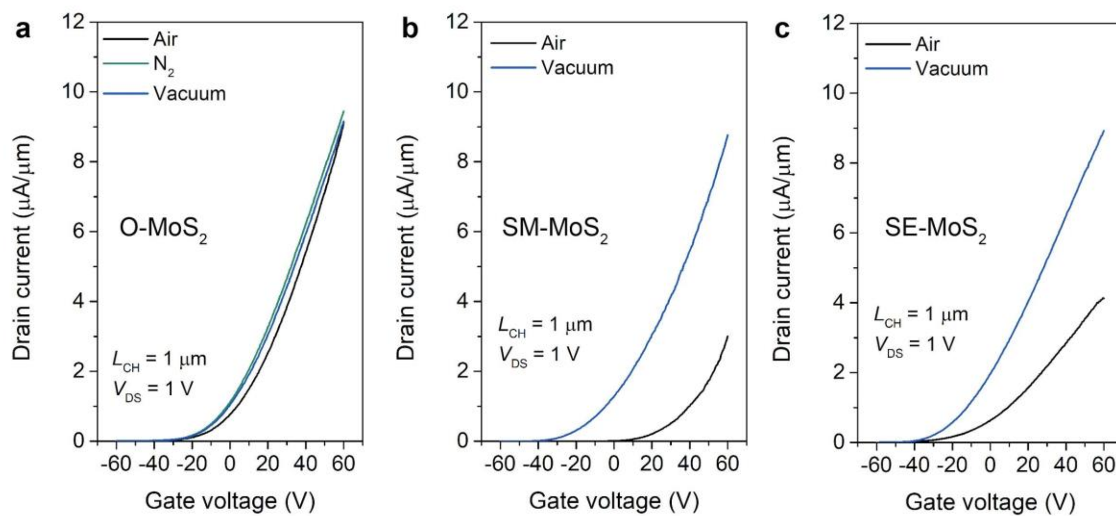

Supplementary Figure 26. Transfer characteristics of different types of MoS_2 devices measured in different environments. **a,** O-MoS_2; **b,** SM-MoS_2; **c,** SE-MoS_2. The discrepancies between the SM- or SE-MoS_2 measured in air and in vacuum are due to the oxygen adsorption/desorption.

14. The effect of electron irradiation on O-MoS_2 in scanning transmission electron microscope (STEM)

We performed the aberration-corrected scanning transmission electron microscope (STEM) at 60 keV to minimize the beam damage of MoS_2. Before the experiment, the sample was baked in high vacuum (~1×10^{-7} torr) at 160 °C overnight to reduce the surface contamination and outgassing. The experiment is performed in Nion UltraSTEM-100 at ultrahigh vacuum (9×10^{-9} mbar). Even though meticulous precaution has been taken, we found that the sample is still susceptible to electron beam with significant beam damage. Figure S27 shows the fast degradation of O-MoS_2 lattice under electron beams, which does not allow a high S/N image to be taken with enough resolution to resolve lattices, especially the configuration of O. The electron beam damage is a common problem for doped TMDs generally, especially in locations that lattice configurations are changed with decreased bond strength.

As a comparison, the SM-MoS_2 sample is much more stable than O-MoS_2 under electron beam irradiation. A comparison can be seen in Figure S27(d), even when the electron beam dose is kept at 1/64 of the beam dose used on a regular MoS_2 sample. This has made it impossible to acquire atomic resolved images for O-MoS_2.

In order to understand the atomic displacement behavior, we have carried out the ab-initio molecular dynamics (MD) to calculate the displacement threshold of a three-coordinated O dopant and a three-coordinated regular S atom in MoS_2. In these simulations, we assign an initial momentum to either the O or the S atom and let the whole system evolve under the frame of ab-initio molecular dynamics. The initial energy is gradually increased until a point where these atoms start to get displaced from the lattice. These energies are marked as the displacement threshold energy. Our results show that the displacement threshold of the O atom is 57 keV, and the S atom is 89 keV when only elastic scattering is considered. The minimum electron voltage in a commonly used STEM is at 60 keV, which is well above the displacement threshold of an O atom, so it is mostly impossible to observe an O atom if the electron beam is parked around it to get a decent signal-to-noise ratio. Also, in this ab-initio MD calculation, we only consider the energy-momentum transfer between electron and an atom (elastic scattering), but no radiolysis effect coming from inelastic scattering is considered. In a semiconductor such as MoS_2, radiolysis effect will also contribute to the displacement of atoms[10], which further lowers down the displacement threshold of an atom under the electron bombardment. This is why S atoms, even with a higher elastic displacement threshold than 60 keV, are still being displaced by STEM. For the same reason,

O dopant atoms in MoS_2 will have an even lower displacement threshold than 57 keV when inelastic scattering is considered, further lowering the possibility of observing O atoms in MoS_2.

On the other hand, the above analysis has explained the much lower tolerance of electron beams on our sample, which provides more evidence showing that the O atom is doped in the MoS_2 lattice.

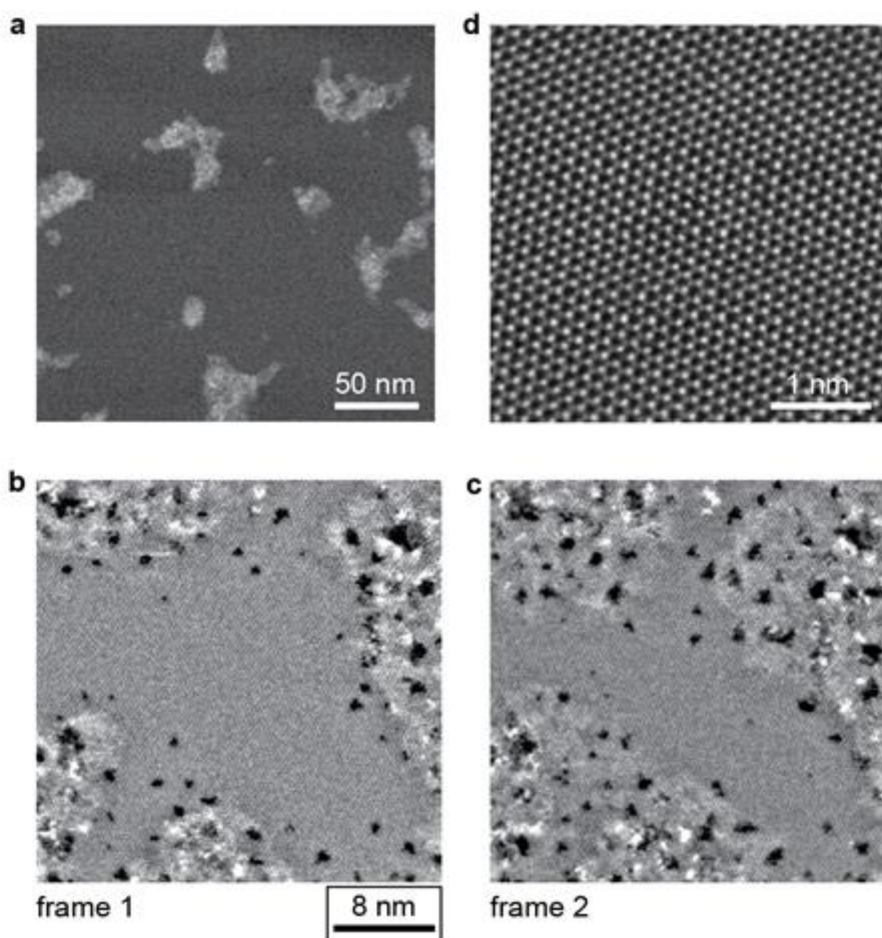

Figure S27. Electron beam damage of O-MoS_2. a, An overview of the O-MoS_2 sample before beam damage. No voids or vacancies can be seen in the field of view. **b,c,** Two consecutive frames on the same location with only 2.1 seconds of beam exposure in each frame. Vacancies and voids are generated at a fast speed. **d,** Atomic-resolved image for SM-MoS_2 taken in the same system with a much smaller field of view as a comparison to the O-MoS_2. The electron irradiation dose is

64 times higher than b and c, while no obvious damage is observed on MoS_2. The four images are all 512 × 512 pixels with a dwell time of 8 μs/pixel. The beam current at the sample is 50-60 pA.

References

1. Ling, X. *et al.* Role of the seeding promoter in MoS2 growth by chemical vapor deposition. *Nano letters* **14**, 464-472 (2014).
2. Michail, A., Delikoukos, N., Parthenios, J., Galiotis, C. & Papagelis, K. Optical detection of strain and doping inhomogeneities in single layer MoS2. *Applied Physics Letters* **108**, 173102 (2016).
3. Rice, C. *et al.* Raman-scattering measurements and first-principles calculations of strain-induced phonon shifts in monolayer MoS 2. *Physical Review B* **87**, 081307 (2013).
4. Conley, H. J. *et al.* Bandgap engineering of strained monolayer and bilayer MoS2. *Nano letters* **13**, 3626-3630 (2013).
5. Lloyd, D. *et al.* Band gap engineering with ultralarge biaxial strains in suspended monolayer MoS2. *Nano letters* **16**, 5836-5841 (2016).
6. Sheng, Y. *et al.* Photoluminescence segmentation within individual hexagonal monolayer tungsten disulfide domains grown by chemical vapor deposition. *ACS Applied Materials & Interfaces* **9**, 15005-15014 (2017).
7. Lilliu, S. *et al.* EFM data mapped into 2D images of tip-sample contact potential difference and capacitance second derivative. *Scientific reports* **3**, 3352 (2013).
8. Sadewasser, S. & Glatzel, T. *Kelvin probe force microscopy*. Vol. 48 (Springer, 2012).
9. Allain, A., Kang, J., Banerjee, K. & Kis, A. Electrical contacts to two-dimensional semiconductors. *Nature materials* **14**, 1195-1205 (2015).
10. Susi, T., Meyer, J. C. & Kotakoski, J. Quantifying transmission electron microscopy irradiation effects using two-dimensional materials. *Nature Reviews Physics* **1**, 397-405 (2019).